Cell Reports



# KSHV infection drives poorly cytotoxic CD56-negative natural killer cell differentiation *in vivo* upon KSHV/EBV dual infection

## Graphical abstract

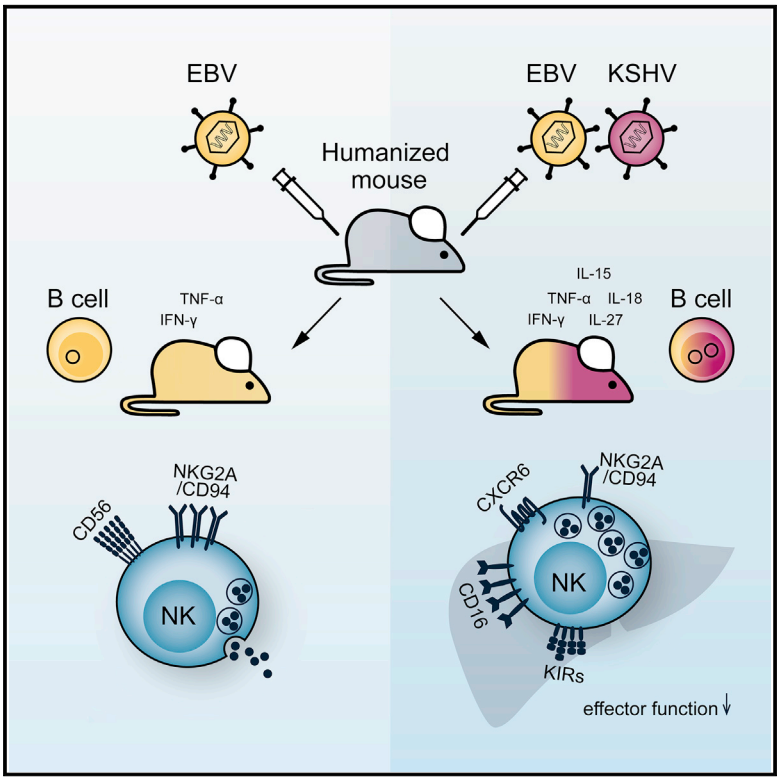


## Highlights

- CD56$^{-}$ CD16$^{+}$ NK cells accumulate upon KSHV/EBV dual infection in humanized mice
- KSHV titers correlate with CD56$^{-}$ CD16$^{+}$ NK cell frequency *in vivo*
- CD56$^{-}$ CD16$^{+}$ NK cells display impaired effector functions

## Authors

Nicole Caduff, Donal McHugh, Lisa Rieble, ..., Obinna Chijioke, Ann M. Moormann, Christian Münz

## Correspondence

christian.muenz@uzh.ch

## In brief

Caduff et al. utilize a humanized mouse model to characterize NK cell responses upon dual infection with the human tumor viruses KSHV and EBV. They describe an increase of dysfunctional CD56$^{-}$CD16$^{+}$ NK cells with KSHV viremia *in vivo* and an accumulation of this subset in KSHV-seropositive children.

Caduff et al., 2021, Cell Reports *35*, 109056
May 4, 2021 
https://doi.org/10.1016/j.celrep.2021.109056

Cell Reports

CellPress
OPEN ACCESS

Report

# KSHV infection drives poorly cytotoxic CD56-negative natural killer cell differentiation *in vivo* upon KSHV/EBV dual infection

Nicole Caduff,[1] Donal McHugh,[1] Lisa Rieble,[1] Catherine S. Forconi,[2] John M. Ong'echa,[3] Peter O. Oluoch,[2,3] Ana Raykova,[1] Anita Murer,[1] Michelle Böni,[1] Lara Zuppiger,[1] Thomas F. Schulz,[4] David J. Blackbourn,[5] Obinna Chijioke,[6] Ann M. Moormann,[2] and Christian Münz[1,7,*]

[1]Viral Immunobiology, Institute of Experimental Immunology, University of Zürich, Zürich, Switzerland
[2]Division of Infectious Diseases, Department of Medicine, University of Massachusetts Medical School, Worcester, MA, USA
[3]Center for Global Health Research, Kenya Medical Research Institute, Kisumu, Kenya
[4]Institute of Virology, Hannover Medical School, Hannover and German Centre of Infection Research (DZIF), Hannover-Braunschweig Site, Hannover, Germany
[5]School of Biosciences and Medicine, University of Surrey, Guildford, UK
[6]Cellular Immunotherapy, Institute of Experimental Immunology, University of Zürich, Zürich, Switzerland
[7]Lead contact
*Correspondence: christian.muenz@uzh.ch
https://doi.org/10.1016/j.celrep.2021.109056

## SUMMARY

Herpesvirus infections shape the human natural killer (NK) cell compartment. While Epstein-Barr virus (EBV) expands immature NKG2A$^+$ NK cells, human cytomegalovirus (CMV) drives accumulation of adaptive NKG2C$^+$ NK cells. Kaposi sarcoma-associated herpesvirus (KSHV) is a close relative of EBV, and both are associated with lymphomas, including primary effusion lymphoma (PEL), which nearly always harbors both viruses. In this study, KSHV dual infection of mice with reconstituted human immune system components leads to the accumulation of CD56$^-$CD16$^+$CD38$^+$CXCR6$^+$ NK cells. CD56$^-$CD16$^+$ NK cells were also more frequently found in KSHV-seropositive Kenyan children. This NK cell subset is poorly cytotoxic against otherwise-NK-cell-susceptible and antibody-opsonized targets. Accordingly, NK cell depletion does not significantly alter KSHV infection in humanized mice. These data suggest that KSHV might escape NK-cell-mediated immune control by driving CD56$^-$CD16$^+$ NK cell differentiation.

## INTRODUCTION

Two of the seven known human tumor viruses belong to the family of γ-herpesviruses (Bouvard et al., 2009; Parkin, 2006). These are Epstein-Barr virus (EBV) and Kaposi sarcoma-associated herpesvirus (KSHV), associated with around 2% of all malignancies in humans (de Martel et al., 2020). While EBV has causal roles in lymphomas as well as epithelial and rare mesenchymal cell malignancies (Münz, 2019; Shannon-Lowe and Rickinson, 2019), KSHV is associated with B cell lymphoproliferative disorders and the eponymous, endothelial-cell-derived Kaposi sarcoma (KS) (Cesarman et al., 2019; Chang et al., 1994). EBV and KSHV are both thought to drive the malignant transformation of B cells in primary effusion lymphoma (PEL), an aggressive type of large B cell lymphoma with plasmablastic features. PEL cell lines are also the only tumor cells in which KSHV persists *in vitro*. All cases of PEL are associated with KSHV, and up to 90% also contain EBV (Cesarman, 2014). Accordingly, KSHV persistence is predominantly observed in mice with reconstituted human immune system components (humanized mice) in the presence of EBV, and these dual-infected mice develop PEL-like tumors (McHugh et al., 2017). In good agreement, EBV and KSHV orthologs are also co-transmitted in monkeys (Bruce et al., 2018), KSHV is primarily found in co-existence with EBV in Cameroonian children (Labo et al., 2019), and EBV supports persistence of B cell infection by KSHV *in vitro* (Faure et al., 2019). Moreover, the high prevalence of EBV in the adult human population (>95%) makes it likely that KSHV co-exists in the presence of EBV in most adult individuals (Dunmire et al., 2018). Thus, any influence of KSHV on human immune compartments should preferably be investigated in the presence of EBV infection.

Despite the strong growth-transforming capacity of EBV and its high prevalence in the human population, very few virus carriers develop associated malignancies (Münz, 2019; Shannon-Lowe and Rickinson, 2019). In most healthy EBV carriers, immune control is thought to prevent the emergence of virus-associated lymphomas, as these can be observed at increased frequencies in patients with immunodeficiencies (Damania and

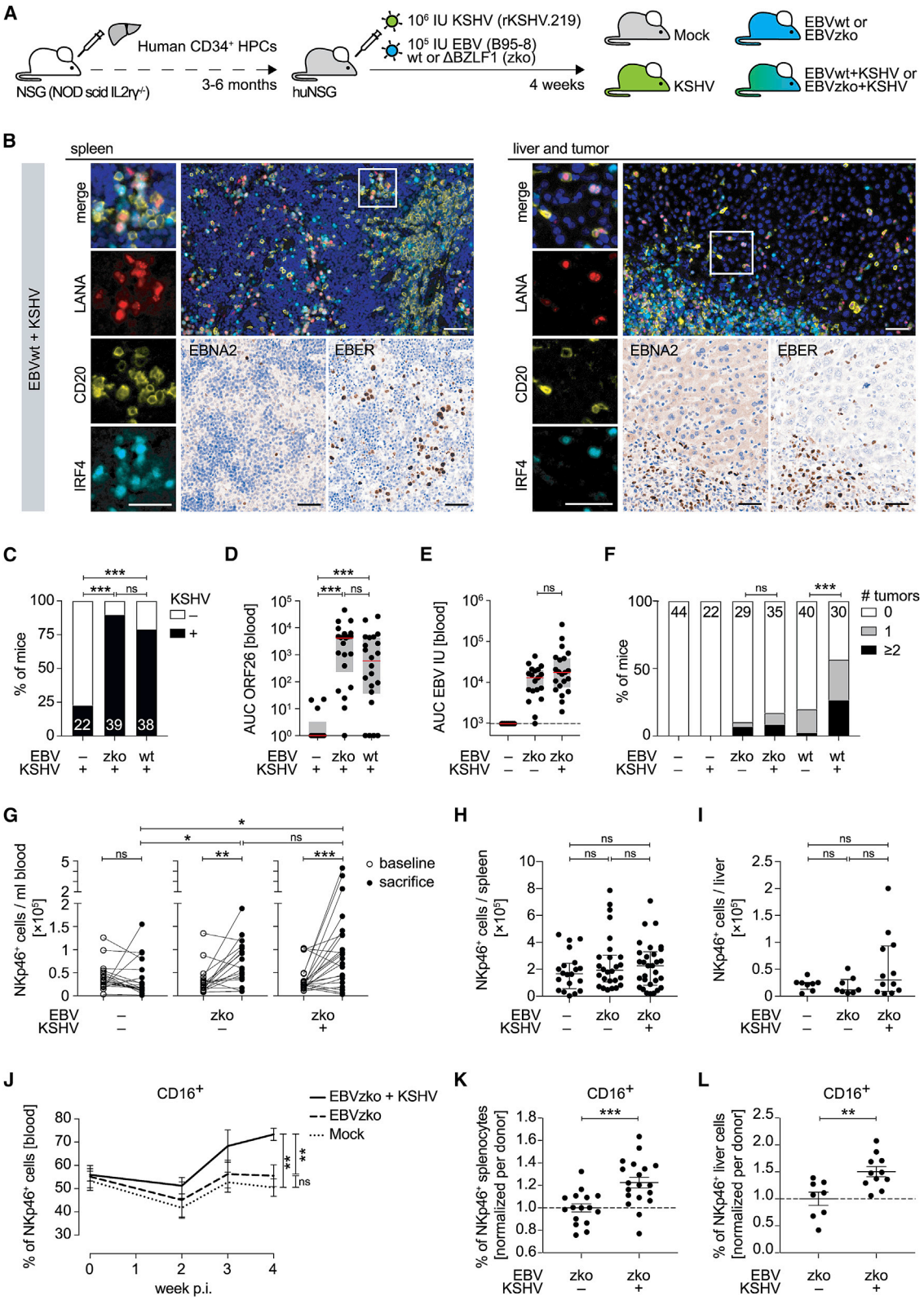


*(legend on next page)*

Münz, 2019; Latour and Fischer, 2019; Totonchy and Cesarman, 2016). Natural killer (NK) cells expand during primary EBV infection, control lytic viral replication in humanized mice, and have been identified as crucial components of EBV-specific immune responses by studying primary immunodeficiencies (Azzi et al., 2014; Chijioke et al., 2013; Dunmire et al., 2015; Landtwing et al., 2016; Münz, 2017; Tangye and Latour, 2020; Williams et al., 2005). NK cell activity against target cells is regulated by the balance of germline-encoded activating versus inhibitory receptors, and despite multiple viral evasion strategies, NK cells are particularly potent in restricting herpesvirus infections (Mancini and Vidal, 2020). They contribute to antiviral immunity via cytokine production, such as interferon (IFN)-γ in response to interleukin (IL)-12, and direct killing of infected cells induced by type I IFNs (Vidal et al., 2011). In order to exert these antiviral immune responses, NK cells often require an IL-15-and IL-18-dependent priming step in secondary lymphoid tissues, reminiscent of $CD8^+$ T cell priming (Chaix et al., 2008; Lucas et al., 2007). In humans, this activation leads to the stepwise differentiation of $CD56^{bright}CD16^-$ to $CD56^{dim}CD16^+$ NK cells that then successively acquire killer-immunoglobulin-like inhibitory receptors (KIRs) (Björkström et al., 2010a; Ferlazzo et al., 2004). At any differentiation step, NK cells can acquire the lymphocytic senescence marker CD57 and stop expanding (Björkström et al., 2010a). In contrast to KSHV, many NK cell functions and differentiation patterns have been characterized during infections with EBV or the β-herpesvirus cytomegalovirus (CMV). Here, we report that KSHV drives $CD56^-CD16^+CD38^+$ NK cell differentiation with a partially tissue-resident (CXCR6, CD69) and immunosuppressive phenotype (CD39) in EBV-co-infected humanized mice. $CD56^-CD16^+$ NK cells are also found to be enriched in KSHV-seropositive children in a Kenyan pediatric cohort, supporting our *in vivo* findings. Although these NK cells retain their cytotoxic machinery, they poorly kill NK cell susceptible targets, even after antibody opsonization.

## RESULTS

### KSHV infection leads to an accumulation of $CD16^+$ NK cells in humanized mice

We investigated the influence of KSHV infection on human NK cells in an *in vivo* model of persistent KSHV infection developed in our laboratory (McHugh et al., 2017) and based on EBV co-infection of NOD-*scid* $IL2R\gamma_c^{-/-}$ (NSG) mice harboring human immune system components. Humanized NSG (huNSG) mice were injected with $10^6$ infectious units (IUs) of KSHV (rKSHV.219) or $10^5$ IUs of EBV (B95-8), both viruses simultaneously or mock-infected with PBS (Figures 1A and S1A). Studies were performed with a lytic replication-deficient EBV strain that lacks BZLF-1 (EBVzko), compared to the wild-type EBV (EBVWT) control, since NK cells mainly control EBV lytically replicating cells (Azzi et al., 2014; Chijioke et al., 2013; Pappworth et al., 2007), and KSHV enhances the lytic activity of EBVWT in huNSG mice (McHugh et al., 2017). Animals were euthanized at 4 weeks post-infection (p.i.) or earlier if they met predetermined humane endpoint criteria, resulting in a significantly reduced survival of dual-infected compared to single- and mock-infected mice (Figure S1B). Spleen and liver sections of infected mice contained $CD20^+$ and $IRF4^+/CD20^{low}$ cells that were positive for the KSHV latency-associated nuclear antigen (LANA) in areas with a similar pattern of EBV-infected cells on adjacent tissue sections, as determined by the presence of the EBV nuclear antigen (EBNA) 2 and the EBV-encoded small RNAs (EBERs) (Figure 1B). These staining patterns support the previously reported infection of $EBV^+$ human B cells with plasma-cell-like phenotype by KSHV in this model (McHugh et al., 2017). The frequency of mice positive for KSHV ORF26 DNA or LANA protein was significantly higher when injected simultaneously with EBV of either strain (Figure 1C; McHugh et al., 2017). Peripheral blood and splenic KSHV DNA loads were similar between EBVWT+KSHV and EBVzko+KSHV mice (Figures 1D and S1C), and EBVzko titers were not affected by KSHV co-infection (Figures 1E and S1D;

**Figure 1. KSHV infection leads to the accumulation of $CD16^+$ NK cells in huNSG mice**

(A) Experimental outline of EBV and KSHV infection in huNSG mice.

(B) Co-staining of LANA with CD20 and IRF4 on splenic and liver sections with tumor of an EBVWT+KSHV mouse by immunofluorescent (IF) staining. EBER *in situ* hybridization (ISH) and EBNA2 immunohistochemistry (IHC) staining are shown below. Scale bar: 50 μm.

(C) Frequency of mice injected with KSHV with evidence of viral infection, based on KSHV DNA detection in the blood and spleen and LANA IHC of tissue sections. 15 independent experiments; total number of mice indicated. Fisher's exact test.

(D and E) Mice without quantifiable viral DNA levels are plotted on (D) the x axis or (E) the dashed line indicating the quantification threshold.

(D) The area under the curve (AUC) of ORF26 copies/ml at weeks 2, 3, and 4 p.i. was computed to depict the longitudinal peripheral blood KSHV burden. Nine independent experiments with n = 14–22 mice per group.

(E) AUC EBV load in international units/ml at weeks 2–4 p.i. depicted for mice of five independent experiments with n = 10–21.

(F) Frequency of mice with no tumor, 1 tumor, and ≥2 macroscopic tumors. 15 independent experiments; total number of mice per group indicated. Mann-Whitney U test (MWU) for comparison of tumor score.

(G) Total numbers of live, human $CD45^+CD3^-NKp46^+$ cells/ml peripheral blood before infection (baseline) and at 4 weeks p.i. (sacrifice) are depicted for individual mice of five independent experiments. Baseline and sacrifice NK cell numbers within groups were analyzed by Wilcoxon test.

(H and I) Total numbers of live, human $CD45^+CD3^-NKp46^+$ cells per (H) spleen or (I) liver. Median, IQR. Composite data from (H) nine independent experiments with n = 20–30 mice per group and (I) two independent experiments with n = 8–12 mice per group.

(J) Frequency of $CD16^+$ within human peripheral blood $CD45^+CD3^-NKp46^+$ cells over time in mock (n = 5), EBVzko (n = 5), and EBVzko+KSHV (n = 6) mice. Statistical analysis was performed with mixed-effects model (REML) followed by Fisher's LSD test. False discovery rate (FDR)-adjusted p (q) values, mean ± SEM.

(K and L) Frequency of human $CD45^+Lin^-$ (CD3, CD19, CD14, CD4) $NKp46^+$ (K) splenocytes or (L) liver cells positive for CD16 of mice from four and two independent experiments, respectively, relative to the mean of the respective EBVzko group.

Mean ± SEM, MWU. *p < 0.05, **p < 0.01, ***p < 0.001. Unless otherwise stated, statistical analysis was performed using Kruskal-Wallis (KW) test followed by Dunn's multiple comparison test with q values indicated.

See also Figure S1.

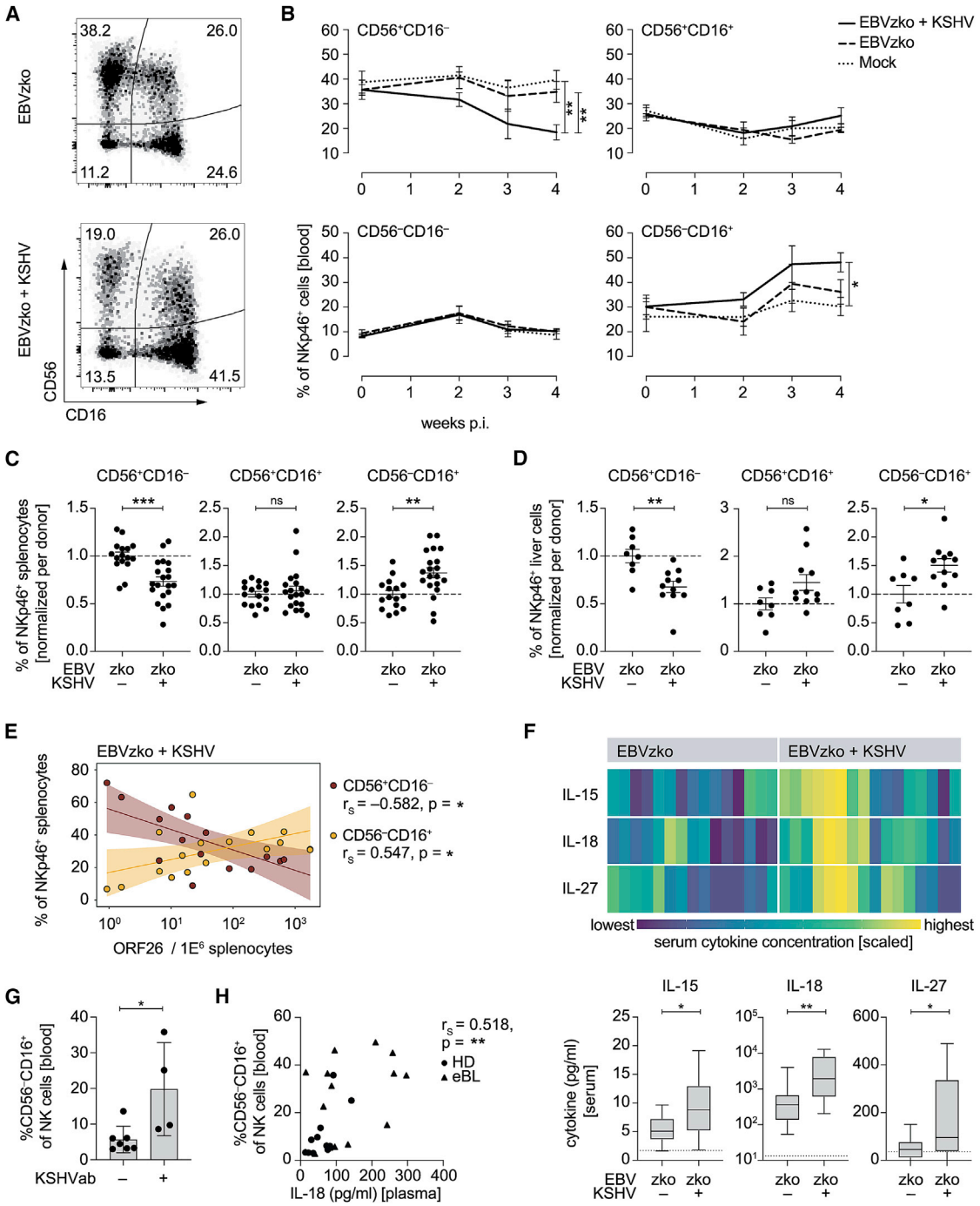


**Figure 2. CD56⁻CD16⁺ NK cells are enriched in the NK cell compartment of KSHV-infected huNSG mice, as well as in Kenyan KSHV-seropositive children**

(A) Representative flow cytometry dot plots of human CD45⁺NKp46⁺Lin⁻ splenocytes of EBVzko and EBVzko+KSHV mice.

(B) Frequency of peripheral blood CD56- and CD16-stained NK cell subsets over time in mock (n = 5), EBVzko (n = 5), and EBVzko+KSHV (n = 6) mice. REML followed by Fisher's LSD test, q values, mean ± SEM.

(C and D) Frequency of CD56- and CD16-stained NK cell subsets among splenic (C) or hepatic (D) CD45⁺CD3⁻NKp46⁺ cells of mice from four and two independent experiments, respectively, relative to the mean of the respective EBVzko group. Mean ± SEM, MWU.

(E) Correlations between splenic KSHV DNA load and the frequency of CD56⁺CD16⁻ (red) and CD56⁻CD16⁺ (yellow) NK cells are depicted for EBVzko+KSHV co-infected mice from four independent experiments. Solid lines represent trend lines obtained by linear regression, and shaded areas indicate 95% confidence interval (CI) of each trend line. Mice with values below 0.1 ORF26 copies per $10^6$ cells were excluded.

*(legend continued on next page)*

McHugh et al., 2017). KSHV infection significantly increased the frequency of mice harboring macroscopic tumors when co-infected with EBVWT as compared to EBVWT single-infected animals, but not in mice co-infected with the EBVzko strain (Figure 1F; McHugh et al., 2017). As such, dual infection of mice with KSHV and EBVzko allows the investigation of persistent KSHV infection without the confounding presence of additional KSHV+EBV-driven tumor formation observed during EBVWT co-infection.

The majority of human NK cells in huNSG mice express the natural cytotoxicity receptor NKp46 (Chijioke et al., 2013; Strowig et al., 2010). Upon infection, peripheral blood human NKp46$^{+}$CD3$^{-}$ NK cell numbers increased, but splenic or hepatic NK cell counts 4 weeks p.i. were similar between EBV single- and EBV+KSHV co-infected animals (Figures 1G–1I). However, we documented an increase in the frequency of CD16$^{+}$ NK cells in the blood of dual-infected mice over time (Figure 1J), and a significantly higher proportion of this subset was also found in spleen and liver of dual-infected mice compared to EBVzko single-infected animals (Figures 1K and 1L). Thus, our data suggest that infection with KSHV leads to an accumulation of the more differentiated CD16$^{+}$ NK cell subset.

## CD56$^{-}$CD16$^{+}$ NK cells are enriched in the NK cell compartment of KSHV-infected humanized mice as well as Kenyan KSHV-seropositive children

In humans, the expression of CD56 and CD16 distinguishes two major subsets: the mainly cytokine-producing CD56$^{bright}$CD16$^{-}$ NK cells and the more cytotoxic CD56$^{dim}$CD16$^{+}$ subset that constitutes the majority of NK cells in human peripheral blood. In naive huNSG mice, the majority of NK cells are CD56$^{+}$CD16$^{-}$, the subset that is considered less mature than its CD16$^{+}$ counterpart (Strowig et al., 2010). Interestingly, the significant increase in CD16$^{+}$ NK cell frequency in EBVzko+KSHV co-infected mice was due to an increase in the frequency of a non-classical CD56$^{-}$CD16$^{+}$ NK cell population at the expense of CD56$^{+}$CD16$^{-}$ cells (Figure 2A). We observed a gradual increase in the frequency of peripheral blood CD56$^{-}$CD16$^{+}$ NK cells over time in EBVzko+KSHV co-infected, but not EBVzko single- or mock-infected, animals (Figure 2B). This difference in the NK cell subset distribution was also observed in the spleen and liver of EBVzko+KSHV co-infected, compared to EBVzko single-infected, animals (Figures 2C and 2D). Within dual-infected animals, KSHV titers positively correlated with the relative abundance of splenic CD56$^{-}$CD16$^{+}$ NK cells, and a negative correlation was observed between splenic KSHV loads and the frequency of CD56$^{+}$CD16$^{-}$ NK cells (Figure 2E). EBV viral loads did not positively correlate with CD56$^{-}$CD16$^{+}$ NK cell frequency (Figure S1E). Concurrently, KSHV co-infected mice had significantly higher serum levels of IL-15, IL-18, and IL-27 (Figure 2F), but not IL-12p70, IL-2, FLT3L, and type I IFNs (Figures S1F and S1G).

In healthy adults, CD56$^{-}$CD16$^{+}$ NK cells are present in very limited numbers (Björkström et al., 2010b). Among healthy Kenyan children, CD56$^{-}$CD16$^{+}$ NK cells were significantly more frequent in KSHV-seropositive compared to seronegative donors (Figure 2G). However, in Kenyan pediatric patients with endemic Burkitt lymphoma (eBL), CD56$^{-}$CD16$^{+}$ NK cell frequency was elevated and not further increased with seropositivity to KSHV (Figure S1H). Nevertheless, CD56$^{-}$CD16$^{+}$ NK cell frequencies correlated with IL-18 serum levels across all tested groups (Figures 2H and S1I). These data suggest that KSHV infection drives CD56$^{-}$CD16$^{+}$ NK cell accumulation in both huNSG mice and the investigated pediatric cohorts, potentially via IL-15, IL-18 and IL-27.

## KSHV infection drives CD56$^{-}$CD16$^{+}$ NK cell differentiation with expression of CD38, CD39, CD69, and CXCR6 in humanized mice

In order to characterize the accumulating CD56$^{-}$CD16$^{+}$ NK cells in more detail, we assessed their maturation and activation status in spleen and liver of EBVzko+KSHV-infected huNSG mice by flow cytometry. Nearly all NKp46$^{+}$Lin$^{-}$ cells co-expressed the pan-NK cell marker CD7, which is not found on mature myeloid cells (Milush et al., 2009), and only a minority of Lin$^{-}$CD7$^{+}$ cells did not express NKp46 (Figures S2A and S2B). After manual gating on human CD45$^{+}$CD7$^{+}$Lin$^{-}$ lymphocytes, uniform manifold approximation and projection (UMAP) was used for dimensionality reduction and visualization of cells (Figures 3A and 3B). CD16$^{+}$ NK cell subsets expressed less NKp46 as well as NKG2A and CD94 (Figure 3C), the two components of an inhibitory C-type lectin receptor, described to be highly expressed by CD56$^{bright}$ NK cells and to decrease during differentiation (Björkström et al., 2010a; Di Vito et al., 2019; Yu et al., 2010) (Figures 3C, S2C, and S3A). Furthermore, CD16$^{+}$ NK cells were largely negative for early NK differentiation and innate lymphoid cell markers CD117 and CD127 (Figures 3D, S2D, and S3B). Inversely, the expression of KIRs and CD57, which are progressively acquired with differentiation, was confined to the CD16$^{+}$ subsets and was similar between CD56$^{+}$CD16$^{+}$ and CD56$^{-}$CD16$^{+}$ cells.

CD56$^{-}$CD16$^{+}$ NK cells less frequently expressed CD2, a co-stimulatory receptor important for the signaling of NKp46 and CD16 (Bryceson et al., 2006; Liu et al., 2016), compared to CD56$^{+}$CD16$^{+}$ NK cells, whereas nearly all CD56$^{-}$CD16$^{+}$ NK cells expressed the activation marker CD38 (Figure 3D). When comparing NK cells from different experimental groups, we observed a significant increase in CD56$^{-}$CD16$^{+}$CD38$^{+}$ cells in EBVzko+KSHV co-infected compared to control mice and a concomitant decrease of CD56$^{+}$CD16$^{-}$CD2$^{+}$CD38$^{-}$ cells

(F) Cytokine concentration was measured in the serum of EBVzko (n = 15) and EBVzko+KSHV (n = 16) mice at 4 weeks p.i. The median (IQR) is shown with minimum and maximum ranges as whiskers. Composite data are from four independent experiments, MWU. Dashed lines indicate lower level of quantification (LLOQ).

(G) Frequency of CD56$^{-}$CD16$^{+}$ NK cells in KSHV-seropositive and KSHV-negative (KSHVab + and –) pediatric healthy donors (HDs). Mean ± SD. MWU.

(H) Correlation between CD56$^{-}$CD16$^{+}$ NK cell frequencies and serum IL-18 in pediatric HDs and eBL patients.

*p < 0.05, **p < 0.01, ***p < 0.001. $r_S$, Spearman's correlation.

See also Figure S1.

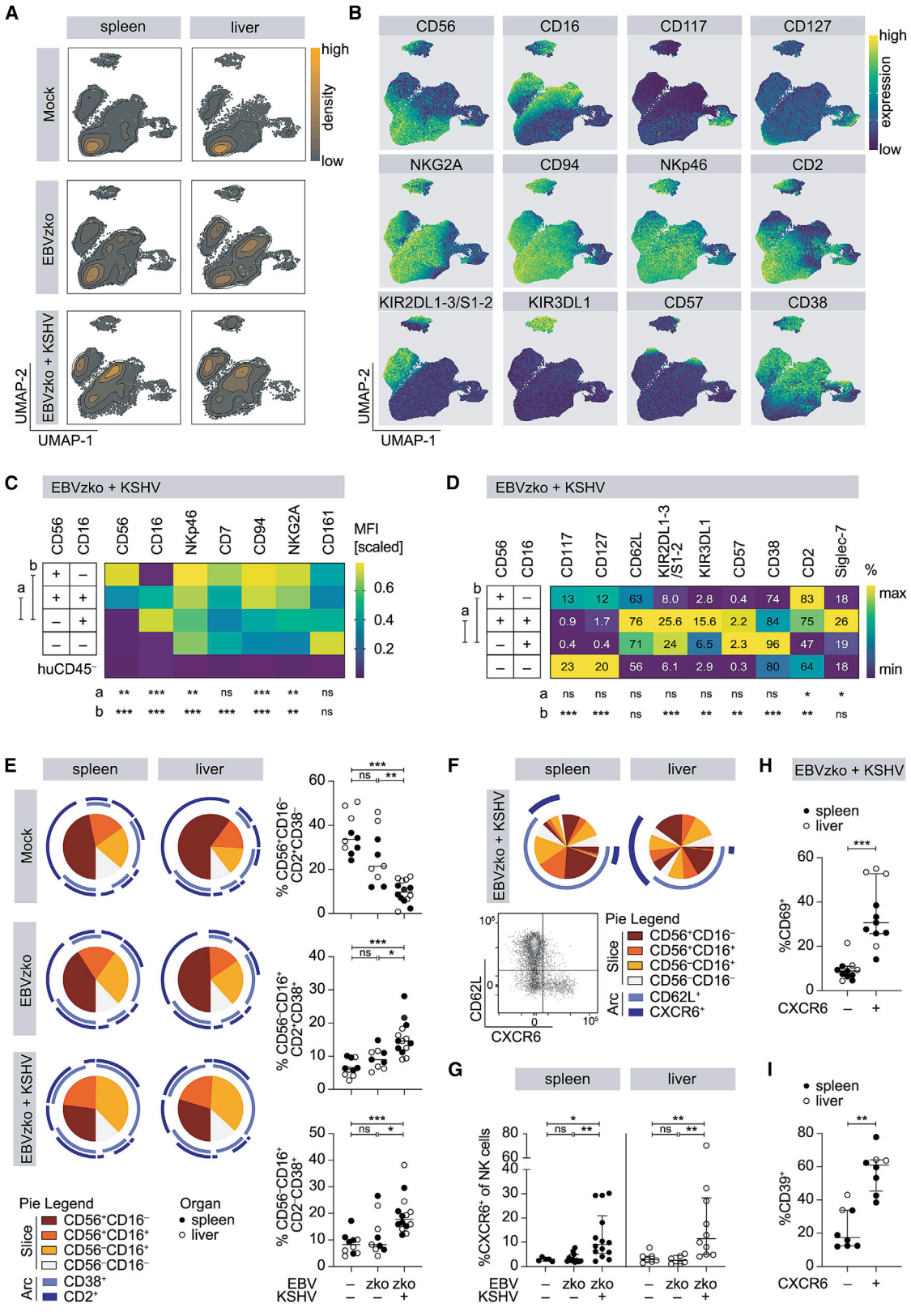


*(legend on next page)*

(Figures 3E and S3C). Furthermore, dual infection with KSHV led to the accumulation of splenic and hepatic NK cells expressing the tissue residency marker CXCR6 (Dogra et al., 2020; Harmon et al., 2016), frequently co-expressing CD69 (Figures 3F–3H, S3D, and S3E). CXCR6 expression further correlated with KSHV titers (Figure S3F). Lastly, CXCR6$^+$ NK cells preferentially co-expressed CD39 (Figure 3I), a cell-surface ATP ectonucleotidase associated with immunosuppression and cell exhaustion (Canale et al., 2018; Tøndell et al., 2020; Wu et al., 2020; Zheng et al., 2020). Thus, KSHV infection seems to promote the expansion of activated, differentiated, and potentially immunosuppressive NK cells with hallmarks of tissue residency *in vivo*.

### KSHV infection increases NK cell cytotoxicity, but CD56$^-$CD16$^+$ NK cells kill poorly even after target cell opsonization

Next, we addressed NK cell functions in KSHV-infected huNSG mice, as hyporesponsiveness to target cells and cytokine stimulation has been described for CD56$^-$CD16$^+$ NK cells (Björkström et al., 2010b). Proliferating (Ki-67$^+$) splenic NK cells at 4 weeks p.i. were significantly more frequent in EBVzko+KSHV co-infected, compared to EBVzko and mock, animals and were preferentially CD56$^+$CD16$^-$CD57$^-$ (Figures 4A and S4A). In line with a more mature phenotype, CD16$^+$ NK cell subsets more frequently contained effector molecules, granzyme B, and/or perforin, compared to the CD16$^-$ counterparts, with the highest perforin levels found in CD56$^-$CD16$^+$ cells (Figures 4B and S4B). Overall, the frequency of perforin-/granzyme-B-expressing NK cells was highest in EBVzko+KSHV mice (Figure 4C), indicating increased activation and "priming" of NK cells upon dual infection. Accordingly, NK cells from EBVzko+KSHV co-infected mice degranulated significantly more frequently against K562 cells compared to NK cells from control mice (Figures 4D, 4E, and S4C). The majority of degranulation occurred, however, among CD56$^+$CD16$^-$ and not in the accumulating CD56$^-$CD16$^+$ NK cell subset (Figure 4F). Although shedding of CD16 upon stimulation, as previously described (Goodier et al., 2016; Romee et al., 2013), may have caused underestimation of CD56$^-$CD16$^+$ NK cell degranulation, the overall poor degranulation of CD56$^-$ subsets against K562 was insufficient to account for the superior performance of NK cells from EBVzko+KSHV mice (Figure S4D). Besides pronounced shedding of CD16 upon contact with opsonized cells (Figures 4G and 4H), degranulation mediated by antibody-dependent cellular cytotoxicity (ADCC) was only slightly increased in EBVzko+KSHV-infected mice (Figures 4D and S4C). Similar to the superior degranulation of CD56$^+$ subsets against K562 targets, CD56$^+$ cells more readily produced IFN-$\gamma$ upon cytokine stimulation (Figure S4E). Furthermore, serum levels of the potentially NK-cell-derived cytokines IFN-$\gamma$ and tumor necrosis factor alpha (TNF-$\alpha$) were increased in both EBVzko- and EBVzko+KSHV-infected, compared to mock-infected, mice (Figures 4I and S4F). Thus, enhanced NK cell activation during KSHV co-infection leads to the accumulation of hyporesponsive CD56$^-$CD16$^+$ NK cells and the increased proliferation, cytokine production, and cytotoxicity of a diminished number of CD56$^+$CD16$^-$ NK cells.

Accordingly, NK cell depletion with an NKp46-specific antibody (Chijioke et al., 2013; Landtwing et al., 2016) did not significantly affect KSHV viral burden, KSHV persistence rate, or tumor formation in huNSG mice (Figures 4J–4M, and S4G–S4I). Altogether, KSHV infection differentiates NK cells toward the CD56$^-$CD16$^+$ subset that, despite its high cytotoxic molecule content, seems to be maintained in a reduced functional state, and the NK cell compartment as a whole is unable to meaningfully control KSHV.

## DISCUSSION

In this study, we have investigated the effect of persistent KSHV infection on the NK cell compartment in humanized mice. We observed an accumulation of CD56$^-$CD16$^+$CD38$^+$CXCR6$^+$ CD69$^+$CD39$^+$ NK cells, which correlated with KSHV viral burden. Likewise, Kenyan KSHV-seropositive children were found to carry higher frequencies of CD56$^-$CD16$^+$ NK cells. This is a quite unique observation among herpesviruses, since infection with the $\alpha$-herpesvirus herpes simplex virus (HSV) does not seem to change the composition of the NK cell repertoire (Björkström et al., 2011), the $\beta$-herpesvirus CMV drives the accumulation of CD56$^+$CD16$^+$NKG2C$^+$KIR$^+$ adaptive NK cells (Gumá et al., 2004; Smith et al., 2020), and the $\gamma$-herpesvirus EBV expands CD56$^+$CD16$^{+/-}$NKG2A$^+$KIR$^-$ NK cells (Azzi et al., 2014). The functional relevance of these compositional changes in the NK cell

**Figure 3. KSHV infection drives CD56$^-$CD16$^+$ NK cell differentiation with expression of CD38, CD39, CD69, and CXCR6 in huNSG mice**

(A) UMAP visualization of single, live, human CD45$^+$Lin$^-$ (CD3, CD19, CD14, CD4) CD7$^+$ cells isolated at 4 weeks p.i. from spleen and liver of mock-, EBVzko-, and EBVzko+KSHV-infected mice depicted as contour plot.

(B) UMAP plot depicting relative marker expression from samples in (A).

(C) Heatmap depicting median fluorescent intensity (MFI) of surface markers on CD56- and CD16-stained NK cell subsets (pre-gated on human CD45$^+$NKp46$^+$Lin$^-$) and on human CD45$^-$ cells of EBVzko+KSHV co-infected animals.

(D) Heatmap depicting the median frequency of cells positive for indicated surface markers among different CD56- and CD16-stained NK cell subsets. In (C) and here, composite data are from 1–4 independent experiments with n = 6–20 animals. Data are normalized per column. Statistical analysis was performed by multiple comparison tests following paired one-way ANOVA or Friedmann's test (q values). See also Figures S3A and S3B.

(E and F) Expression of (E) CD38 and CD2 or (F) CXCR6 and CD62L among splenic and hepatic NK cells. Colors in the pie charts indicate CD56/CD16 subsets. Pie arc colors depict the expression of (E) CD38 and CD2 or (F) CXCR6 and CD62L. In (E), scatterplots depict subset frequencies within NKp46$^+$ cells of individual mice (symbol color: black, spleen; clear, liver). Median.

(G) Frequencies of CXCR6$^+$ splenic or hepatic NK cells.

(H and I) Frequencies of cells expressing (H) CD69 or (I) CD39 among CXCR6$^+$ and CXCR6$^-$ NK cells from EBVzko+KSHV mice. Wilcoxon test.

In (G)–(I), three independent experiments. Median (IQR). In (C)–(I), NK cells were pre-gated on huCD45$^+$, live, Lin$^-$ (CD3, CD19, CD14, CD4) NKp46$^+$ cells. *$p < 0.05$, **$p < 0.01$, ***$p < 0.001$. Unless otherwise stated, statistical analysis was performed by Dunn's test following KW test (q values).

See also Figures S2 and S3.

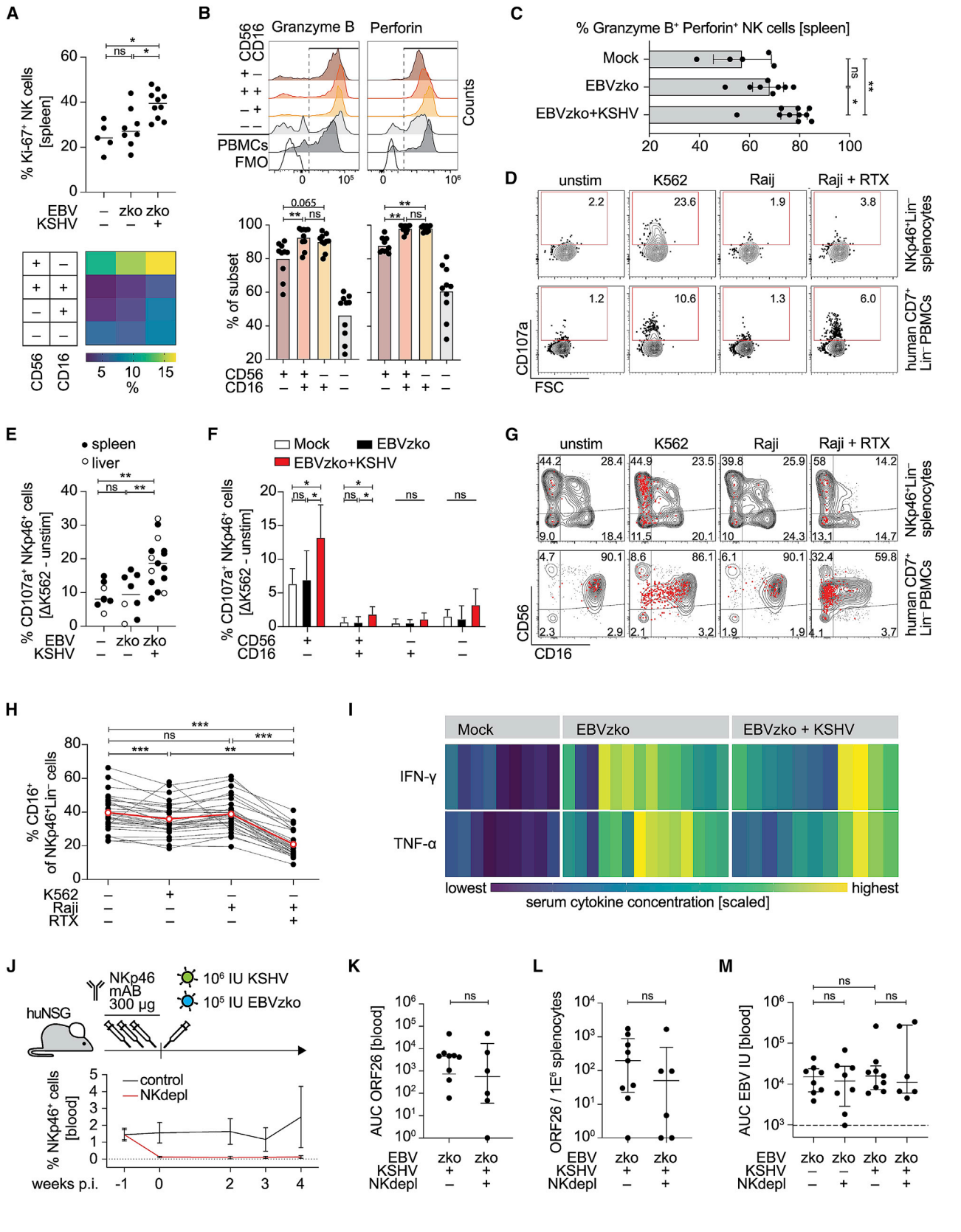


*(legend on next page)*

repertoire for the immune control of viruses, however, often remains unclear.

Along these lines, it had originally been suggested that NK cells can kill KSHV-infected cells (Lebbé et al., 1997; Matthews et al., 2011; Sirianni et al., 2002). However, NK cell cytotoxicity is reduced in patients with KSHV-associated malignancies, in part via downregulation of activating NK cell receptors and increased expression of inhibitory receptors (Beldi-Ferchiou et al., 2016; Dupuy et al., 2012; Sirianni et al., 2005). While many immune escape mechanisms have been described for CMV (Mancini and Vidal, 2020), NK cell responses are protective against infection with this β-herpesvirus in preclinical *in vivo* models. In contrast, we report that the accumulation of poorly cytotoxic $CD56^{-}CD16^{+}$ NK cells during KSHV infection is associated with a lack of NK-cell-mediated immune control of this γ-herpesvirus infection *in vivo*. We show that antibody-mediated NK cell depletion, which compromises immune control of EBVWT infection in the same humanized mouse model (Chijioke et al., 2013; Landtwing et al., 2016), does not lead to increased KSHV titers or more frequent persistent KSHV infection. Thus, the decreased *in vitro* cytotoxicity of $CD56^{-}CD16^{+}$ $CD38^{+}CXCR6^{+}$ NK cells that accumulate during KSHV infection in humanized mice is in line with their inability to control this γ-herpesvirus *in vivo*.

In good agreement, $CD56^{-}CD16^{+}$ NK cells display compromised functions during other chronic viral infections despite phenotypically resembling $CD56^{+}CD16^{+}$ NK cells in many aspects (Björkström et al., 2010b; Forconi et al., 2018, 2020; Milush et al., 2013; Müller-Durovic et al., 2019; Voigt et al., 2018). $CD56^{-}CD16^{+}$ NK cell numbers increase with HIV-viremia and decrease upon successful antiretroviral therapy (Alter et al., 2005; Mavilio et al., 2005; Milush et al., 2013). $CD56^{-}CD16^{+}$ NK cells also accumulate in elderly people co-infected with EBV and CMV (Müller-Durovic et al., 2019) and in pediatric patients with $EBV^{+}$ post-transplant lymphoproliferative disease (Wiesmayr et al., 2012) or eBL (Forconi et al., 2018). The latter association might, however, also result from holoendemic malaria exposure (Forconi et al., 2018), which is itself associated with KSHV seropositivity (Nalwoga et al., 2015; Oluoch et al., 2020). While it is difficult to control and account for multiple pathogens or underlying health issues during natural infection in humans where exposure cannot be assigned, studies in humanized mice allow the investigation of single parameters or a combination thereof, facilitating the interpretation of likely causes and consequences of $CD56^{-}CD16^{+}$ NK cell accumulation. At the same time, *de novo* infections in huNSG mice may not allow the study of long-term effects of chronic infection or tumorigenesis.

A pro-inflammatory environment common to all these conditions, either by one virus or by a combination of pathogens, might drive $CD56^{-}CD16^{+}$ NK cell differentiation. The cytokines IL-15, IL-18, and IL-27, identified to be elevated upon KSHV and EBV co-infection in this study, are good candidates to drive this differentiation, and their role should be investigated in future studies. Moreover, NK cell differentiation by KSHV is associated with upregulation of molecules that facilitate tissue residency, like CXCR6 and CD69 (Freud et al., 2017), accompanied by immunosuppressive CD39 expression. Thus, KSHV might escape NK-cell-mediated immune control by reducing cytotoxicity and patrolling patterns of these innate lymphocytes, with potential relevance in the development of KS and PEL, which predominantly occur in the context of HIV co-infection.

## STAR★METHODS

Detailed methods are provided in the online version of this paper and include the following:

- KEY RESOURCES TABLE
- RESOURCE AVAILABILITY
  - Lead contact
  - Materials availability
  - Data and code availability

**Figure 4. KSHV infection increases NK cell cytotoxicity, but $CD56^{-}CD16^{+}$ NK cells kill poorly even after target cell opsonization**

(A) Frequency of splenic Ki-$67^{+}$ NK cells of individual mice from two independent experiments. Median. Heatmap depicts median frequencies upon sub-gating on CD56- and CD16-stained NK cell subsets.

(B) Representative MFI histograms of granzyme B and perforin expression within huNSG splenic NK cell subsets isolated at 4 weeks p.i. compared to NK cells from human peripheral blood mononuclear cells (PBMCs) and fluorescence minus one (FMO) controls. Scatterplots depict frequencies of granzyme $B^{+}$ and $perforin^{+}$ splenocytes among subsets from EBVzko+KSHV mice of two independent experiments.

(C) Frequency of NK cells dual positive for granzyme B and perforin. Median (IQR).

In (D)–(H), ex vivo degranulation assays at 4 weeks p.i. are shown. (D) Representative contour plots of the CD107a staining upon co-culture of huNSG splenocytes (top) or human PBMCs (bottom) with K562 cells, Raji cells, Raji cells + rituximab (RTX), or medium (unstimulated control). HuNSG NK cells were pre-gated on live $huCD45^{+}Lin^{-}$ $NKp46^{+}$ cells; human PBMCs were gated on live $huCD45^{+}Lin^{-}CD7^{+}$ cells.

(E and F) Specific degranulation of NK cells from (E) different experimental groups and (F) upon sub-gating on NK populations, as measured by the frequency of $CD107a^{+}$ cells upon contact with K562 minus background (unstimulated control). Two independent experiments. (E) Median. (F) Mean +SD.

(G) Representative flow cytometry contour plots of CD56 and CD16 expression upon co-culture as in (D). $CD107a^{+}$ cells are overlaid as red dots.

(H) Frequency of $CD16^{+}$ NK cells ($Lin^{-}NKp46^{+}$) after co-culture as in (D). Connected dots represent individual mice. Mean is shown in red. Friedman's test (q values).

(I) Serum cytokine concentration at 4 weeks p.i. of mock (n = 9), EBVzko (n = 14), and EBVzko+KSHV (n = 11) mice from five independent experiments (heatmap values scaled per row).

(J) Experimental outline of NK cell depletion experiments (n = 2) and frequency of peripheral blood $huCD45^{+}CD3^{-}NKp46^{+}$ cells over time. Mean ± SEM.

(K and L) AUC of (K) peripheral blood KSHV ORF26 DNA levels (weeks 2–4 p.i.) and (L) at 4 weeks p.i. in the spleen. Median (IQR), MWU.

(M) AUC (weeks 2-4 p.i.) of peripheral blood EBV international units/ml. Median (IQR), MWU.

$^{*}p < 0.05$, $^{**}p < 0.01$, $^{***}p < 0.001$. Unless otherwise stated, statistical analysis was performed by Dunn's test following KW test (q values).

See also Figure S4.

## SUPPLEMENTAL INFORMATION

Supplemental information can be found online at https://doi.org/10.1016/j.celrep.2021.109056.

## ACKNOWLEDGMENTS

This research was supported in part by Cancer Research Switzerland, Switzerland (KFS-4091-02-2017); KFSP-PrecisionMS and HMZ ImmunoTargET of the University of Zurich, Switzerland; the Cancer Research Center Zurich, Switzerland; the Vontobel Foundation, Switzerland; the Baugarten Foundation, Switzerland; the Sobek Foundation, Germany; the Swiss Vaccine Research Institute, Switzerland; Roche, Switzerland; Novartis, Switzerland; and the Swiss National Science Foundation, Switzerland (310030B_182827 and CRSII5_180323). A.M.M. was funded by a National Institutes of Health, United States, grant (R01 CA189806). N.C. was supported by a career advancement grant from the University of Zurich, Switzerland (FK-18-026). D.M. and M.B. were supported by MD-PhD fellowships from the Swiss National Science Foundation, Switzerland, and the Swiss Academy of Medical Sciences, Switzerland (323530_145247 and 323630_19938).

## AUTHOR CONTRIBUTIONS

Conceptualization, N.C. and C.M.; formal analysis, N.C. and C.S.F.; investigation, N.C., D.M., L.R., C.S.F., J.M.O., P.O.O., A.R., A.M., M.B., and L.Z.; resources, T.F.S., D.J.B., A.M.M., and C.M.; writing – original draft, N.C. and C.M.; writing – review & editing, D.M., L.R., C.S.F., J.M.O., P.O.O., A.R., A.M., M.B., L.Z., T.F.S., D.J.B., O.C., and A.M.M.; visualization, N.C.; supervision, C.M. and A.M.M; funding acquisition, N.C., D.M., A.M.M., and C.M.

## DECLARATION OF INTERESTS

The authors declare no competing interests.

Received: September 1, 2020
Revised: January 29, 2021
Accepted: April 8, 2021
Published: May 4, 2021

## REFERENCES

Alter, G., Teigen, N., Davis, B.T., Addo, M.M., Suscovich, T.J., Waring, M.T., Streeck, H., Johnston, M.N., Staller, K.D., Zaman, M.T., et al. (2005). Sequential deregulation of NK cell subset distribution and function starting in acute HIV-1 infection. Blood *106*, 3366–3369.

Antsiferova, O., Müller, A., Rämer, P.C., Chijioke, O., Chatterjee, B., Raykova, A., Planas, R., Sospedra, M., Shumilov, A., Tsai, M.-H., et al. (2014). Adoptive transfer of EBV specific CD8$^+$ T cell clones can transiently control EBV infection in humanized mice. PLoS Pathog. *10*, e1004333.

Azzi, T., Lünemann, A., Murer, A., Ueda, S., Béziat, V., Malmberg, K.-J., Staubli, G., Gysin, C., Berger, C., Münz, C., et al. (2014). Role for early-differentiated natural killer cells in infectious mononucleosis. Blood *124*, 2533–2543.

Barter, R.L., and Yu, B. (2018). Superheat: An R package for creating beautiful and extendable heatmaps for visualizing complex data. J. Comput. Graph. Stat. *27*, 910–922.

Beldi-Ferchiou, A., Lambert, M., Dogniaux, S., Vély, F., Vivier, E., Olive, D., Dupuy, S., Levasseur, F., Zucman, D., Lebbé, C., et al. (2016). PD-1 mediates functional exhaustion of activated NK cells in patients with Kaposi sarcoma. Oncotarget *7*, 72961–72977.

Berger, C., Day, P., Meier, G., Zingg, W., Bossart, W., and Nadal, D. (2001). Dynamics of Epstein-Barr virus DNA levels in serum during EBV-associated disease. J. Med. Virol. *64*, 505–512.

Björkström, N.K., Riese, P., Heuts, F., Andersson, S., Fauriat, C., Ivarsson, M.A., Björklund, A.T., Flodström-Tullberg, M., Michaëlsson, J., Rottenberg, M.E., et al. (2010a). Expression patterns of NKG2A, KIR, and CD57 define a process of CD56dim NK-cell differentiation uncoupled from NK-cell education. Blood *116*, 3853–3864.

Björkström, N.K., Ljunggren, H.-G., and Sandberg, J.K. (2010b). CD56 negative NK cells: origin, function, and role in chronic viral disease. Trends Immunol. *31*, 401–406.

Björkström, N.K., Svensson, A., Malmberg, K.-J., Eriksson, K., and Ljunggren, H.-G. (2011). Characterization of natural killer cell phenotype and function during recurrent human HSV-2 infection. PLoS ONE *6*, e27664.

Bouvard, V., Baan, R., Straif, K., Grosse, Y., Secretan, B., El Ghissassi, F., Benbrahim-Tallaa, L., Guha, N., Freeman, C., Galichet, L., and Cogliano, V.; WHO International Agency for Research on Cancer Monograph Working Group (2009). A review of human carcinogens–Part B: biological agents. Lancet Oncol. *10*, 321–322.

Bruce, A.G., Barcy, S., Staheli, J., Bielefeldt-Ohmann, H., Ikoma, M., Howard, K., and Rose, T.M. (2018). Experimental co-transmission of Simian Immunodeficiency Virus (SIV) and the macaque homologs of the Kaposi Sarcoma-Associated Herpesvirus (KSHV) and Epstein-Barr Virus (EBV). PLoS ONE *13*, e0205632.

Bryceson, Y.T., March, M.E., Ljunggren, H.G., and Long, E.O. (2006). Synergy among receptors on resting NK cells for the activation of natural cytotoxicity and cytokine secretion. Blood *107*, 159–166.

Canale, F.P., Ramello, M.C., Núñez, N., Araujo Furlan, C.L., Bossio, S.N., Gorosito Serrán, M., Tosello Boari, J., Del Castillo, A., Ledesma, M., Sedlik, C., et al. (2018). CD39 expression defines cell exhaustion in tumor-infiltrating CD8$^+$ T cells. Cancer Res. *78*, 115–128.

Cesarman, E. (2014). Gammaherpesviruses and lymphoproliferative disorders. Annu. Rev. Pathol. *9*, 349–372.

Cesarman, E., Damania, B., Krown, S.E., Martin, J., Bower, M., and Whitby, D. (2019). Kaposi sarcoma. Nat. Rev. Dis. Primers *5*, 9.

Chaix, J., Tessmer, M.S., Hoebe, K., Fuséri, N., Ryffel, B., Dalod, M., Alexopoulou, L., Beutler, B., Brossay, L., Vivier, E., and Walzer, T. (2008). Cutting edge: Priming of NK cells by IL-18. J. Immunol. *181*, 1627–1631.

Chang, Y., Cesarman, E., Pessin, M.S., Lee, F., Culpepper, J., Knowles, D.M., and Moore, P.S. (1994). Identification of herpesvirus-like DNA sequences in AIDS-associated Kaposi's sarcoma. Science *266*, 1865–1869.

Chijioke, O., Müller, A., Feederle, R., Barros, M.H.M., Krieg, C., Emmel, V., Marcenaro, E., Leung, C.S., Antsiferova, O., Landtwing, V., et al. (2013). Human natural killer cells prevent infectious mononucleosis features by targeting lytic Epstein-Barr virus infection. Cell Rep. *5*, 1489–1498.

Damania, B., and Münz, C. (2019). Immunodeficiencies that predispose to pathologies by human oncogenic γ-herpesviruses. FEMS Microbiol. Rev. *43*, 181–192.

de Martel, C., Georges, D., Bray, F., Ferlay, J., and Clifford, G.M. (2020). Global burden of cancer attributable to infections in 2018: a worldwide incidence analysis. Lancet Glob. Health *8*, e180–e190.

Delecluse, H.J., Hilsendegen, T., Pich, D., Zeidler, R., and Hammerschmidt, W. (1998). Propagation and recovery of intact, infectious Epstein-Barr virus from prokaryotic to human cells. Proc. Natl. Acad. Sci. USA *95*, 8245–8250.

Di Vito, C., Mikulak, J., and Mavilio, D. (2019). On the Way to Become a Natural Killer Cell. Front. Immunol. *10*, 1812.

Dogra, P., Rancan, C., Ma, W., Toth, M., Senda, T., Carpenter, D.J., Kubota, M., Matsumoto, R., Thapa, P., Szabo, P.A., et al. (2020). Tissue Determinants of Human NK Cell Development, Function, and Residence. Cell *180*, 749–763.e13.

Dunmire, S.K., Grimm, J.M., Schmeling, D.O., Balfour, H.H., Jr., and Hogquist, K.A. (2015). The Incubation Period of Primary Epstein-Barr Virus Infection: Viral Dynamics and Immunologic Events. PLoS Pathog. *11*, e1005286.

Dunmire, S.K., Verghese, P.S., and Balfour, H.H., Jr. (2018). Primary Epstein-Barr virus infection. J. Clin. Virol. *102*, 84–92.

Dupuy, S., Lambert, M., Zucman, D., Choukem, S.-P., Tognarelli, S., Pages, C., Lebbé, C., and Caillat-Zucman, S. (2012). Human Herpesvirus 8 (HHV8) sequentially shapes the NK cell repertoire during the course of asymptomatic infection and Kaposi sarcoma. PLoS Pathog. *8*, e1002486.

Faure, A., Hayes, M., and Sugden, B. (2019). How Kaposi's sarcoma-associated herpesvirus stably transforms peripheral B cells towards lymphomagenesis. Proc. Natl. Acad. Sci. USA *116*, 16519–16528.

Feederle, R., Kost, M., Baumann, M., Janz, A., Drouet, E., Hammerschmidt, W., and Delecluse, H.J. (2000). The Epstein-Barr virus lytic program is controlled by the co-operative functions of two transactivators. EMBO J. *19*, 3080–3089.

Ferlazzo, G., Thomas, D., Lin, S.-L., Goodman, K., Morandi, B., Muller, W.A., Moretta, A., and Münz, C. (2004). The abundant NK cells in human secondary lymphoid tissues require activation to express killer cell Ig-like receptors and become cytolytic. J. Immunol. *172*, 1455–1462.

Forconi, C.S., Cosgrove, C.P., Saikumar-Lakshmi, P., Nixon, C.E., Foley, J., Ong'echa, J.M., Otieno, J.A., Alter, G., Münz, C., and Moormann, A.M. (2018). Poorly cytotoxic terminally differentiated $CD56^{neg}CD16^{pos}$ NK cells accumulate in Kenyan children with Burkitt lymphomas. Blood Adv. *2*, 1101–1114.

Forconi, C.S., Oduor, C.I., Oluoch, P.O., Ong'echa, J.M., Münz, C., Bailey, J.A., and Moormann, A.M. (2020). A New Hope for $CD56^{neg}CD16^{pos}$ NK Cells as Unconventional Cytotoxic Mediators: An Adaptation to Chronic Diseases. Front. Cell. Infect. Microbiol. *10*, 162.

Freud, A.G., Mundy-Bosse, B.L., Yu, J., and Caligiuri, M.A. (2017). The Broad Spectrum of Human Natural Killer Cell Diversity. Immunity *47*, 820–833.

Galili, T., O'Callaghan, A., Sidi, J., and Sievert, C. (2018). heatmaply: an R package for creating interactive cluster heatmaps for online publishing. Bioinformatics *34*, 1600–1602.

Goodier, M.R., Lusa, C., Sherratt, S., Rodriguez-Galan, A., Behrens, R., and Riley, E.M. (2016). Sustained Immune Complex-Mediated Reduction in CD16 Expression after Vaccination Regulates NK Cell Function. Front. Immunol. *7*, 384.

Greiner, M., Pfeiffer, D., and Smith, R.D. (2000). Principles and practical application of the receiver-operating characteristic analysis for diagnostic tests. Prev. Vet. Med. *45*, 23–41. https://doi.org/10.1016/S0167-5877(00)00115-X.

Gumá, M., Angulo, A., Vilches, C., Gómez-Lozano, N., Malats, N., and López-Botet, M. (2004). Imprint of human cytomegalovirus infection on the NK cell receptor repertoire. Blood *104*, 3664–3671.

Harmon, C., Robinson, M.W., Fahey, R., Whelan, S., Houlihan, D.D., Geoghegan, J., and O'Farrelly, C. (2016). Tissue-resident $Eomes^{(hi)}$ $T\text{-}bet^{(lo)}$ $CD56^{(bright)}$ NK cells with reduced proinflammatory potential are enriched in the adult human liver. Eur. J. Immunol. *46*, 2111–2120.

Hartmann, F.J., Bernard-Valnet, R., Quériault, C., Mrdjen, D., Weber, L.M., Galli, E., Krieg, C., Robinson, M.D., Nguyen, X.H., Dauvilliers, Y., et al. (2016). High-dimensional single-cell analysis reveals the immune signature of narcolepsy. J. Exp. Med. *213*, 2621–2633.

Kati, S., Tsao, E.H., Günther, T., Weidner-Glunde, M., Rothämel, T., Grundhoff, A., Kellam, P., and Schulz, T.F. (2013). Activation of the B cell antigen receptor triggers reactivation of latent Kaposi's sarcoma-associated herpesvirus in B cells. J. Virol. *87*, 8004–8016.

Kati, S., Hage, E., Mynarek, M., Ganzenmueller, T., Indenbirken, D., Grundhoff, A., and Schulz, T.F. (2015). Generation of high-titre virus stocks using BrK.219, a B-cell line infected stably with recombinant Kaposi's sarcoma-associated herpesvirus. J. Virol. Methods *217*, 79–86.

Labo, N., Marshall, V., Miley, W., Davis, E., McCann, B., Stolka, K.B., Ndom, P., Hemingway-Foday, J.J., Abassora, M., Newton, R., et al. (2019). Mutual detection of Kaposi's sarcoma-associated herpesvirus and Epstein-Barr virus in blood and saliva of Cameroonians with and without Kaposi's sarcoma. Int. J. Cancer *145*, 2468–2477.

Landtwing, V., Raykova, A., Pezzino, G., Béziat, V., Marcenaro, E., Graf, C., Moretta, A., Capaul, R., Zbinden, A., Ferlazzo, G., et al. (2016). Cognate HLA absence in trans diminishes human NK cell education. J. Clin. Invest. *126*, 3772–3782.

Latour, S., and Fischer, A. (2019). Signaling pathways involved in the T-cell-mediated immunity against Epstein-Barr virus: Lessons from genetic diseases. Immunol. Rev. *291*, 174–189.

Lebbé, C., de Crémoux, P., Millot, G., Podgorniak, M.P., Verola, O., Berger, R., Morel, P., and Calvo, F. (1997). Characterization of in vitro culture of HIV-negative Kaposi's sarcoma-derived cells. In vitro responses to alfa interferon. Arch. Dermatol. Res. *289*, 421–428.

Liu, L.L., Landskron, J., Ask, E.H., Enqvist, M., Sohlberg, E., Traherne, J.A., Hammer, Q., Goodridge, J.P., Larsson, S., Jayaraman, J., et al. (2016). Critical Role of CD2 Co-stimulation in Adaptive Natural Killer Cell Responses Revealed in NKG2C-Deficient Humans. Cell Rep. *15*, 1088–1099.

Lucas, M., Schachterle, W., Oberle, K., Aichele, P., and Diefenbach, A. (2007). Dendritic cells prime natural killer cells by trans-presenting interleukin 15. Immunity *26*, 503–517.

Mancini, M., and Vidal, S.M. (2020). Mechanisms of Natural Killer Cell Evasion Through Viral Adaptation. Annu. Rev. Immunol. *38*, 511–539.

Matthews, N.C., Goodier, M.R., Robey, R.C., Bower, M., and Gotch, F.M. (2011). Killing of Kaposi's sarcoma-associated herpesvirus-infected fibroblasts during latent infection by activated natural killer cells. Eur. J. Immunol. *41*, 1958–1968.

Mavilio, D., Lombardo, G., Benjamin, J., Kim, D., Follman, D., Marcenaro, E., O'Shea, M.A., Kinter, A., Kovacs, C., Moretta, A., and Fauci, A.S. (2005). Characterization of $CD56^{-}/CD16^{+}$ natural killer (NK) cells: a highly dysfunctional NK subset expanded in HIV-infected viremic individuals. Proc. Natl. Acad. Sci. USA *102*, 2886–2891.

McHugh, D., Caduff, N., Barros, M.H.M., Rämer, P.C., Raykova, A., Murer, A., Landtwing, V., Quast, I., Styles, C.T., Spohn, M., et al. (2017). Persistent KSHV Infection Increases EBV-Associated Tumor Formation In Vivo via Enhanced EBV Lytic Gene Expression. Cell Host Microbe *22*, 61–73.e7.

McHugh, D., Myburgh, R., Caduff, N., Spohn, M., Kok, Y.L., Keller, C.W., Murer, A., Chatterjee, B., Rühl, J., Engelmann, C., et al. (2020). EBV renders B cells susceptible to HIV-1 in humanized mice. Life Sci. Alliance *3*, e202000640.

McInnes, L., Healy, J., and Melville, J. (2018). UMAP: Uniform Manifold Approximation and Projection for Dimension Reduction. arXiv, arXiv:1802.03426.

Meyer, M., Höls, A.-K., Liersch, B., Leistner, R., Gellert, K., Schalke, B., Marx, A., and Niedobitek, G. (2011). Lack of evidence for Epstein-Barr virus infection in myasthenia gravis thymus. Ann. Neurol. *70*, 515–518.

Milush, J.M., Long, B.R., Snyder-Cappione, J.E., Cappione, A.J., 3rd, York, V.A., Ndhlovu, L.C., Lanier, L.L., Michaëlsson, J., and Nixon, D.F. (2009). Functionally distinct subsets of human NK cells and monocyte/DC-like cells identified by coexpression of CD56, CD7, and CD4. Blood *114*, 4823–4831.

Milush, J.M., López-Vergès, S., York, V.A., Deeks, S.G., Martin, J.N., Hecht, F.M., Lanier, L.L., and Nixon, D.F. (2013). $CD56negCD16^{+}$ NK cells are activated mature NK cells with impaired effector function during HIV-1 infection. Retrovirology *10*, 158.

Moormann, A.M., Chelimo, K., Sumba, O.P., Lutzke, M.L., Ploutz-Snyder, R., Newton, D., Kazura, J., and Rochford, R. (2005). Exposure to holoendemic malaria results in elevated Epstein-Barr virus loads in children. J. Infect. Dis. *191*, 1233–1238.

Müller-Durovic, B., Grählert, J., Devine, O.P., Akbar, A.N., and Hess, C. (2019). CD56-negative NK cells with impaired effector function expand in CMV and EBV co-infected healthy donors with age. Aging (Albany NY) *11*, 724–740.

Münz, C. (2017). Humanized mouse models for Epstein Barr virus infection. Curr. Opin. Virol. *25*, 113–118.

Münz, C. (2019). Latency and lytic replication in Epstein-Barr virus-associated oncogenesis. Nat. Rev. Microbiol. *17*, 691–700.

Murer, A., McHugh, D., Caduff, N., Kalchschmidt, J., Barros, M., Zbinden, A., Capaul, R., Niedobitek, G., Allday, M., Chijioke, O., and Münz, C. (2018). EBV persistence without its EBNA3A and 3C oncogenes in vivo. PLoS Pathog. *14*, e1007039.

Nalwoga, A., Cose, S., Wakeham, K., Miley, W., Ndibazza, J., Drakeley, C., Elliott, A., Whitby, D., and Newton, R. (2015). Association between malaria exposure and Kaposi's sarcoma-associated herpes virus seropositivity in Uganda. Trop. Med. Int. Health *20*, 665–672.

Oluoch, P.O., Oduor, C.I., Forconi, C.S., Ong'echa, J.M., Münz, C., Dittmer, D.P., Bailey, J.A., and Moormann, A.M. (2020). Kaposi Sarcoma-Associated Herpesvirus Infection and Endemic Burkitt Lymphoma. J. Infect. Dis. *222*, 111–120.

Pappworth, I.Y., Wang, E.C., and Rowe, M. (2007). The switch from latent to productive infection in epstein-barr virus-infected B cells is associated with sensitization to NK cell killing. J. Virol. *81*, 474–482.

Parkin, D.M. (2006). The global health burden of infection-associated cancers in the year 2002. Int. J. Cancer *118*, 3030–3044.

R Core Team (2020). R: The R Project for Statistical Computing (R Found. Stat. Comput).

Roederer, M., Nozzi, J.L., and Nason, M.C. (2011). SPICE: Exploration and analysis of post-cytometric complex multivariate datasets. Cytometry A *79*, 167–174.

Romee, R., Foley, B., Lenvik, T., Wang, Y., Zhang, B., Ankarlo, D., Luo, X., Cooley, S., Verneris, M., Walcheck, B., and Miller, J. (2013). NK cell CD16 surface expression and function is regulated by a disintegrin and metalloprotease-17 (ADAM17). Blood *121*, 3599–3608.

Shannon-Lowe, C., and Rickinson, A. (2019). The Global Landscape of EBV-Associated Tumors. Front. Oncol. *9*, 713.

Sirianni, M.C., Vincenzi, L., Topino, S., Giovannetti, A., Mazzetta, F., Libi, F., Scaramuzzi, D., Andreoni, M., Pinter, E., Baccarini, S., et al. (2002). NK cell activity controls human herpesvirus 8 latent infection and is restored upon highly active antiretroviral therapy in AIDS patients with regressing Kaposi's sarcoma. Eur. J. Immunol. *32*, 2711–2720.

Sirianni, M.C., Libi, F., Campagna, M., Rossi, D., Capello, D., Sciaranghella, G., Carbone, A., Simonelli, C., Monini, P., Gaidano, G., and Ensoli, B. (2005). Downregulation of the major histocompatibility complex class I molecules by human herpesvirus type 8 and impaired natural killer cell activity in primary effusion lymphoma development. Br. J. Haematol. *130*, 92–95.

Smith, S.L., Kennedy, P.R., Stacey, K.B., Worboys, J.D., Yarwood, A., Seo, S., Solloa, E.H., Mistretta, B., Chatterjee, S.S., Gunaratne, P., et al. (2020). Diversity of peripheral blood human NK cells identified by single-cell RNA sequencing. Blood Adv. *4*, 1388–1406.

Strowig, T., Gurer, C., Ploss, A., Liu, Y.-F., Arrey, F., Sashihara, J., Koo, G., Rice, C.M., Young, J.W., Chadburn, A., et al. (2009). Priming of protective T cell responses against virus-induced tumors in mice with human immune system components. J. Exp. Med. *206*, 1423–1434.

Strowig, T., Chijioke, O., Carrega, P., Arrey, F., Meixlsperger, S., Rämer, P.C., Ferlazzo, G., and Münz, C. (2010). Human NK cells of mice with reconstituted human immune system components require preactivation to acquire functional competence. Blood *116*, 4158–4167.

Tangye, S.G., and Latour, S. (2020). Primary immunodeficiencies reveal the molecular requirements for effective host defense against EBV infection. Blood *135*, 644–655.

Tedeschi, R., Enbom, M., Bidoli, E., Linde, A., De Paoli, P., and Dillner, J. (2001). Viral load of human herpesvirus 8 in peripheral blood of human immunodeficiency virus-infected patients with Kaposi's sarcoma. J. Clin. Microbiol. *39*, 4269–4273.

Tøndell, A., Wahl, S.G.F., Sponaas, A.M., Sørhaug, S., Børset, M., and Haug, M. (2020). Ectonucleotidase CD39 and Checkpoint Signalling Receptor Programmed Death 1 are Highly Elevated in Intratumoral Immune Cells in Non-small-cell Lung Cancer. Transl. Oncol. *13*, 17–24.

Totonchy, J., and Cesarman, E. (2016). Does persistent HIV replication explain continued lymphoma incidence in the era of effective antiretroviral therapy? Curr. Opin. Virol. *20*, 71–77.

Vidal, S.M., Khakoo, S.I., and Biron, C.A. (2011). Natural killer cell responses during viral infections: flexibility and conditioning of innate immunity by experience. Curr. Opin. Virol. *1*, 497–512.

Vieira, J., and O'Hearn, P.M. (2004). Use of the red fluorescent protein as a marker of Kaposi's sarcoma-associated herpesvirus lytic gene expression. Virology *325*, 225–240.

Voigt, J., Malone, D.F.G., Dias, J., Leeansyah, E., Björkström, N.K., Ljunggren, H.-G., Gröbe, L., Klawonn, F., Heyner, M., Sandberg, J.K., and Jänsch, L. (2018). Proteome analysis of human $CD56^{neg}$ NK cells reveals a homogeneous phenotype surprisingly similar to $CD56^{dim}$ NK cells. Eur. J. Immunol. *48*, 1456–1469.

White, R.E., Rämer, P.C., Naresh, K.N., Meixlsperger, S., Pinaud, L., Rooney, C., Savoldo, B., Coutinho, R., Bödör, C., Gribben, J., et al. (2012). EBNA3B-deficient EBV promotes B cell lymphomagenesis in humanized mice and is found in human tumors. J. Clin. Invest. *122*, 1487–1502.

Wiesmayr, S., Webber, S.A., Macedo, C., Popescu, I., Smith, L., Luce, J., and Metes, D. (2012). Decreased NKp46 and NKG2D and elevated PD-1 are associated with altered NK-cell function in pediatric transplant patients with PTLD. Eur. J. Immunol. *42*, 541–550.

Williams, H., McAulay, K., Macsween, K.F., Gallacher, N.J., Higgins, C.D., Harrison, N., Swerdlow, A.J., and Crawford, D.H. (2005). The immune response to primary EBV infection: a role for natural killer cells. Br. J. Haematol. *129*, 266–274.

Wu, J., Wang, Y.C., Xu, W.H., Luo, W.J., Wan, F.N., Zhang, H.L., Ye, D.W., Qu, Y.Y., and Zhu, Y.P. (2020). High expression of CD39 is associated with poor prognosis and immune infiltrates in clear cell renal cell carcinoma. OncoTargets Ther. *13*, 10453–10464.

Yu, J., Mao, H.C., Wei, M., Hughes, T., Zhang, J., Park, I.K., Liu, S., McClory, S., Marcucci, G., Trotta, R., and Caligiuri, M.A. (2010). CD94 surface density identifies a functional intermediary between the $CD56^{bright}$ and $CD56^{dim}$ human NK-cell subsets. Blood *115*, 274–281.

Zheng, Y., Li, Y., Tang, B., Zhao, Q., Wang, D., Liu, Y., Guo, M., Zhao, S., Qi, Y., Zhang, Y., and Huang, L. (2020). IL-6-induced CD39 expression on tumor-infiltrating NK cells predicts poor prognosis in esophageal squamous cell carcinoma. Cancer Immunol. Immunother. *69*, 2371–2380.

## STAR★METHODS

### KEY RESOURCES TABLE

| REAGENT or RESOURCE | SOURCE | IDENTIFIER |
|---|---|---|
| Antibodies | | |
| BUV395 mouse anti-human CD45 (Clone: HI30) | BD Bioscience | Cat#563792; RRID:AB_2744400 |
| BUV563 mouse anti-human CD56 (Clone: NCAM16.2) | BD Bioscience | Cat#565705; RRID:AB_2744431 |
| BUV737 mouse anti-human CD16 (Clone: 3G8) | BD Bioscience | Cat#612786; RRID:AB_2833077 |
| BUV805 mouse anti-human CD69 (Clone: FN50) | BD Bioscience | Cat#748763; RRID:AB_2857327 |
| PB mouse anti-human CD45 (Clone: HI30) | BioLegend | Cat#304029; RRID:AB_2174123 |
| BV421 mouse-anti human CD69 (Clone: FN50) | Biolegend | Cat# 310929 RRID:AB_10933255 |
| BV421 mouse anti-human Perforin (Clone: dG9) | Biolegend | Cat#308122; RRID:AB_2566204 |
| BV421 mouse anti-human CD94 (Clone: HP-3D9) | BD Bioscience | Cat#743948; RRID:AB_2741870 |
| BV421 mouse anti-human CD3 (Clone: UCHT1) | Biolegend | Cat#300434 RRID:AB_10962690 |
| BV421 mouse anti-human CD14 (Clone: HCD14) | Biolegend | Cat#325628 RRID:AB_2563296 |
| BV510 mouse anti-human CD16 (Clone 3G8) | Biolegend | Cat# 302048; RRID: AB_2562085 |
| BV510 mouse anti-human CD3 (Clone: UCHT1) | Biolegend | Cat#300448; RRID:AB_2563468 |
| BV510 mouse anti-human CD4 (Clone: OKT4) | Biolegend | Cat#317444; RRID:AB_2561866 |
| BV510 mouse anti-human CD19 (Clone: HIB19) | Biolegend | Cat#302242; RRID:AB_2561668 |
| BV510 mouse anti-human CD14 (Clone: M5E2) | Biolegend | Cat#301842; RRID:AB_2561946 |
| BV605 mouse anti-human Ki-67 (Clone: Ki-67) | Biolegend | Cat#350522; RRID:AB_2563863 |
| BV605 mouse anti-human CD117 (Clone: 104D2) | Biolegend | Cat#313218; RRID:AB_2562025 |
| BV605 mouse anti-human CD39 (Clone A1) | Biolegend | Cat#328235; RRID: AB_2750429 |
| BV605 mouse anti-human CD4 (Clone: OKT4) | Biolegend | Cat#317438; RRID:AB_11218995 |
| BV711 mouse anti-human CD7 (Clone: M-T701) | BD Bioscience | Cat#564018; RRID:AB_2738544 |
| BV711 mouse anti-human Ki-67 (Clone: Ki-67) | Biolegend | Cat#350516; RRID:AB_2563861 |
| BV786 mouse anti-human CD161 (Clone: DX12) | BD Bioscience | Cat#744096; RRID:AB_2741990 |
| BV786 mouse anti-human IFN-γ (Clone: 4S.B3) | BD Bioscience | Cat#563731; RRID:AB_2738391 |
| BV785 mouse anti-human CD3 (Clone: OKT3) | Biolegend | Cat#317330; RRID:AB_2563507 |

(*Continued on next page*)

*Continued*

| REAGENT or RESOURCE | SOURCE | IDENTIFIER |
|---|---|---|
| FITC mouse anti-human CD94 (Clone: DX22) | Biolegend | Cat#305504; RRID:AB_314534 |
| FITC mouse anti-human CD2 (Clone: RPA-2.10) | Biolegend | Cat#300206; RRID:AB_314030 |
| FITC mouse anti-human CD107a (Clone: H4A3) | BD Bioscience | Cat#555800; RRID:AB_396134 |
| FITC mouse anti-human CD158a,h,g (Clone: HP-MA4) | Biolegend | Cat#339504; RRID:AB_2130378 |
| FITC mouse anti-human CD158b (Clone: DX27) | Biolegend | Cat#312604; RRID:AB_2296486 |
| FITC mouse anti-human CD3 (Clone: UCHT1) | Biolegend | Cat#300406; RRID: AB_314060 |
| PerCp mouse anti-human CD8 (Clone: SK1) | Biolegend | Cat#344708; RRID:AB_1967149 |
| PE mouse anti-human CD159a/NKG2A (Clone: Z199) | Beckman Coulter | Cat#IM3291U; RRID:AB_10643228 |
| PE mouse anti-human CD328/Siglec-7 (Clone: 6-434) | Biolegend | Cat#339204; RRID:AB_1501160 |
| PE mouse anti-human CD19 (Clone: HIB19) | Biolegend | Cat#302208; RRID:AB_314238 |
| PE/Dazzle 594 mouse anti-human CD186/CXCR6 (Clone: K041E5) | Biolegend | Cat#356016; RRID:AB_2563974 |
| PE/Dazzle 594 mouse anti-human CD57 (Clone: HNK-1) | Biolegend | Cat#359620; RRID:AB_2564063 |
| PE/Dazzle 594 mouse anti-human CD127 (Clone: A019D5) | Biolegend | Cat#351336; RRID:AB_2563637 |
| PE-Cy5.5 mouse anti-human CD158a,h (Clone: EB6B) | Beckman Coulter | Cat#A66898; RRID:AB_2857330 |
| PE-Cy5.5 mouse anti-human CD158b1/b2,j-PC5.5 (Clone: GL183) | Beckman Coulter | Cat#A66900; RRID:AB_2857331 |
| PE-Cy7 mouse anti-human CD38 (Clone: HB7) | BD Bioscience | Cat#335790; RRID:AB_399969 |
| PE-Cy7 mouse anti-human TNF-α (Clone: MAb11) | BD Bioscience | Cat#557647; RRID:AB_396764 |
| PE-Cy7 mouse anti-human CD56 (Clone: NCAM16.2) | BD Bioscience | Cat#335826; RRID:AB_2857328 |
| PE-Cy7 mouse anti-human Nkp46 (Clone: 9E2) | BD Bioscience | Cat#562101, RRID:AB_10894195 |
| APC mouse anti-human NKp46 (Clone: 9E2) | BD Bioscience | Cat#558051; RRID:AB_398653 |
| Alexa Fluor 700 mouse anti-human Granzyme B (Clone: GB11) | BD Bioscience | Cat#560213; RRID:AB_1645453 |
| Alexa Fluor 700 mouse anti-human CD19 (Clone: HIB19) | Biolegend | Cat#302226; RRID:AB_493751 |
| Alexa Fluor 700 mouse anti-human CD158e1 (Clone: DX9) | Biolegend | Cat#312712; RRID:AB_2130824 |
| APC-Cy7 mouse anti-human CD16 (Clone: 3G8) | Biolegend | Cat#302018; RRID:AB_314218 |
| APC-Cy7 mouse anti-human CD127 (Clone: A019D5) | Biolegend | Cat#351348; RRID:AB_2629572 |
| APC-Cy7 mouse anti-human CD62L (Clone: DREG-56) | Biolegend | Cat#304814; RRID:AB_493582 |

(*Continued on next page*)

*Continued*

| REAGENT or RESOURCE | SOURCE | IDENTIFIER |
|---|---|---|
| APC-Cy7 mouse anti-human CD4 (Clone: RPA-T4) | Biolegend | Cat# 300518; RRID:AB_314086 |
| Mouse anti-EBNA2 (Clone: PE2) | Abcam | Cat#ab90543; RRID:AB_2049594 |
| Rat anti-LANA (Clone: LN53) | CliniSciences | Cat#Mob395; RRID:AB_2860565 |
| Rabbit anti-human CD20 (Clone: SP32) | Cell Marque | Cat#120R-16; RRID:AB_2860563 |
| Mouse anti-IRF4/MUM1 (Clone: MUM1p) | CliniSciences | Cat#Mob420; RRID:AB_2861384 |
| Purified anti-human NKp46 (Clone: BAB281) | Beckman Coulter | Custom Purified Bulk Antibody (IMBULK1C) |
| Goat anti-human IgM-UNLB (polyclonal) | Southern Biotech | Cat# 2020-01 RRID:AB_2795599 |
| Rituximab | Roche Pharma (Schweiz) AG | MabThera |
| **Bacterial and virus strains** | | |
| EBV B95-8-GFP (EBVwt) produced in HEK293 | Delecluse et al., 1998 | N/A |
| EBV B95-8-BZLF1KO-GFP (EBVzko) produced in HEK293 | Feederle et al., 2000 | N/A |
| rKSHV.219 | Vieira and O'Hearn, 2004; Kati et al., 2015 | N/A |
| **Biological samples** | | |
| Human Fetal Liver samples | Advanced Bioscience Resources | N/A |
| **Chemicals, peptides, and recombinant proteins** | | |
| Zombie Aqua Fixable Viability Dye | Biolegend | Cat#423102 |
| Zombie NIR Fixable Viability Dye | Biolegend | Cat#423106 |
| LIVE/DEAD Fixable Blue Dead Cell Stain Kit | ThermoFisher Scientific | Cat#L23105 |
| TPA (12-O-Tetradecanoylphorbol 13-acetate) | Sigma-Aldrich | Cat#P1585 |
| Recombinant human IL12 p70 | Peprotech | Cat#200-12 |
| Recombinant Human IL-18 | Biolegend | Cat#592102 |
| TAPI-1 (ADAM-17 (TACE) and MMP inhibitor) | Tocris | Cat#6162 |
| **Critical commercial assays** | | |
| DNeasy Blood & Tissue Kit | QIAGEN | Cat#69506 |
| MSD U-plex Biomarker Group 1 (Human) | Meso Scale Discovery | Cat#K15067L |
| MSD V-PLEX Proinflammatroy Panel 1 Human Kit | Meso Scale Discovery | Cat#K15049D |
| IL-18 Human ProcartaPlex Simplex Kit | ThermoFisher Scientific | Cat#EPX01A-10267-901 |
| **Experimental models: Cell lines** | | |
| Brk.219 | Kati et al., 2013 | N/A |
| **Experimental models: Organisms/strains** | | |
| NOD.Cg-*Prkdc*$^{scid}$ *Il2rg*$^{tm1Wjl}$/SzJ (NSG mice) | The Jackson Laboratory | Stock#005557 |
| NOD.Cg-*Mcph1*$^{Tg(HLA-A2.1)1Enge}$ *Prkdc*$^{scid}$ *Il2rg*$^{tm1Wjl}$/SzJ (NSG-A2 mice) | The Jackson Laboratory | Stock#009617 |
| **Oligonucleotides** | | |
| EBV BamHI forward primer: 5′-CTTCTCAGTCCAGCGCGTTT-3′ | modified from Berger et al. (2001) | N/A |

(*Continued on next page*)

*Continued*

| REAGENT or RESOURCE | SOURCE | IDENTIFIER |
|---|---|---|
| EBV BamHI reverse primer:5′-CAGT GGTCCCCCTCCCTAGA-3′ | modified from Berger et al. (2001) | N/A |
| EBV BamHI probe:5′-(FAM)-CGTA AGCCAGACAGCAGCCAATTGT CAG-(TAMRA)-3′ | modified from Berger et al. (2001) | N/A |
| KSHV ORF26 forward primer: 5′-GCTCGAATCCAACGGATTTG-3′ | modified from Tedeschi et al. (2001) | N/A |
| KSHV ORF26 reverse primer: 5′-AATAGCGTGCCCCAGTTGC-3 | modified from Tedeschi et al. (2001) | N/A |
| KSHV ORF26 probe: 5′-(FAM)-TTCCCCATGGTCGTGC CTC-(BHQ-1)-3′ | modified from Tedeschi et al. (2001) | N/A |
| Software and algorithms | | |
| R (v3.6.3) | R Core Team | https://www.r-project.org |
| RStudio (v1.2.5033) | RStudio | https://www.rstudio.com |
| FlowJo (v10.6.2) | FlowJo | https://www.flowjo.com |
| inform (v2.4.8) | PerkinElmer | N/A |
| Phenochart (v1.0) | PerkinElmer | N/A |
| Vectra 3.0 | PerkinElmer | N/A |
| Prism (v8.4.3) | GraphPad Software | https://www.graphpad.com:443/ |
| SPICE - Simplified Presentation of Incredibly Complex Evaluations | Roederer et al., 2011 | https://niaid.github.io/spice |

## RESOURCE AVAILABILITY

### Lead contact

Further information and requests for resources and reagents should be directed to and will be fulfilled by Prof. Christian Münz, PhD (christian.muenz@uzh.ch).

### Materials availability

This study did not generate new unique reagents.

### Data and code availability

This study did not generate datasets or codes.

## EXPERIMENTAL MODEL AND SUBJECT DETAILS

### Human tissue and blood samples

The ethical approval for the use of human fetal liver tissue as well as peripheral blood samples of healthy adult volunteers were obtained from the cantonal ethical committee of Zurich, Switzerland (protocol no. KEK-StV-Nr.19/08). Studies involving peripheral blood of healthy children and pediatric endemic Burkitt lymphoma (eBL) patients in Kenya, described previously in Forconi et al. (2018) and Oluoch et al. (2020), were reviewed and approved by the Scientific and Ethics Review Unit at the Kenya Medical Research Institute, Kenya, and the Institutional Review Board at the University of Massachusetts Medical School, USA. Written informed consent was obtained from parents of pediatric study participants prior to study inclusion. Samples from 14 children with eBL (median age 5.8 years; 64% male) and 11 children without eBL (median age 6 years; 72% male) were used for this study. All subjects were HIV-negative and born to HIV-negative mothers.

### Humanized mouse generation and infection

NOD-*scid* $\gamma c^{-/-}$ mice (NOD.Cg-*Prkdc*$^{scid}$ *Il2rg*$^{tm1Wjl}$/SzJ or NSG) and HLA-A2 transgenic NSG (NOD.Cg-*Mcph1*$^{Tg(HLA-A2.1)1Enge}$ *Prkdc*$^{scid}$ *Il2rg*$^{tm1Wjl}$/SzJ or NSG-A2) mice were purchased from The Jackson Laboratory and bred and maintained at the Institute of Experimental Immunology, University of Zurich. At 1-5 days of age and 5-7 hours after sub-lethal irradiation (1Gy), mice were injected intrahepatically with 1-3 × $10^5$ human fetal liver (HFL)-derived hematopoietic progenitor cells (HPCs). HFL tissue was obtained from Advanced Bioscience Resources, and HPCs were isolated by magnetic cell sorting for CD34 positive cells according to the manufacturer's instructions (Miltenyi Biotec) and as previously described (Strowig et al., 2009; White et al., 2012). Three months after

HPC injection and again one week before infection, the reconstitution of human cells was assessed in the peripheral blood of mice by flow cytometry for human CD45 (huCD45), huCD3, huCD19, huCD4, huCD8 and huNKp46 as previously described (McHugh et al., 2020). Three to six months after engraftment (average: 4.3 months), mice were injected intraperitoneally (i.p.) with $10^6$ HEK293T-Infectious Units (IU) of KSHV (rKSHV.219), $10^5$ Raji IU of EBV (B95-8), simultaneously injected with both viruses or mock-infected with PBS. Apart from tail blood vessel puncture, mice were not involved in any procedures prior to the infection with EBV and KSHV, with the exception of animals that were part of NK cell depletion experiments. These mice received i.p. injections of 100μg purified anti-NKp46 antibody (clone BAB281) in PBS, or mock-injections with PBS, on three consecutive days (total of 300μg per mouse) as previously described (Chijioke et al., 2013). The following day, after assessing the depletion efficiency in peripheral blood by flow cytometry, mice were infected with EBV and KSHV as described. Mice were euthanized at four weeks p.i. or earlier if the predetermined humane endpoint criteria of the laboratory's animal welfare protocol were met that included weight loss (loss of 20% of body weight from maximum weight or 15% persisting for two days) and a scoring for signs of general health and distress (e.g., hunched posture, piloerection, inactivity, grimace). The frequency of macroscopic tumors was assessed by a score: no tumors observed = 0; one tumor observed = 1; multiple tumors observed = 2. EBV-inoculated mice without detectable EBV (BamHI W fragment) DNA in the blood or spleen, and no positive signal for EBNA2 staining or EBER ISH in FFPE tissue sections were considered non-infected and excluded from this study. Similarly, EBV+KSHV-inoculated mice without detectable KSHV (ORF26) DNA in the blood or spleen, and no positive signal for LANA in FFPE tissue sections were considered KSHV non-infected and excluded.

This study includes data from mice reconstituted with $CD34^+$ HPCs isolated from a total of 15 different HFL donors; 13 reconstituted NSG cohorts with 190 animals and 2 reconstituted NSG-A2 cohorts with 36 animals. Individual experiments were performed with a single cohort consisting of mice reconstituted with cells from the same HFL. Mice were distributed to experimental groups under consideration of the sex and frequencies of human cells in the peripheral blood, ensuring a similar sex-ratio and overall similar human immune cell reconstitution between the groups. Investigators were not blinded regarding the grouping of mice. Experiments comprise a total of 137 female mice (Mean weight ± SD: 20.3g ± 1.7g) and 89 male mice (26.3 ± 3.2g) of 20.2 ± 4.7 weeks of age (Mean ± SD; range: 13-29 weeks). The median frequency (and IQR: $25^{th}$, $75^{th}$ percentile) of $huCD45^+$ cells of peripheral blood lymphocytes before infection was 82% (70.5%, 87.1%), $huCD3^+$ T cells of $huCD45^+$ lymphocytes: 33.6% (24.3%, 49.2%), $huCD19^+$ B cells of $huCD45^+$ lymphocytes: 58.1% (42.8%, 67.6%), $huCD4^+$ cells of $huCD3^+$ $huCD45^+$ lymphocytes: 72% (65.4%, 79%), $huCD8^+$ cells of $huCD3^+$ $huCD45^+$ lymphocytes: 24.1% (19%, 30.9%), $CD3^-$ $NKp46^+$ NK cells of human $huCD45^+$ lymphocytes: 1.9% (1.4%, 2.7%) (Figure S1A). Animals were housed in groups and kept singly only in exceptional circumstances (e.g., due to aggressive behavior or absence of male littermates). Animal protocols were reviewed and approved by the veterinary office of the canton of Zurich, Switzerland (116/2008, 148/2011, 209/2014, 159/2017).

## METHOD DETAILS

### Recombinant EBV and KSHV

EBV B95-8-GFP (EBVwt, p2089) and EBV B95-8 ΔBZLF1 -GFP (EBVzko) were produced in HEK293 cells as described previously (Delecluse et al., 1998; Feederle et al., 2000). Recombinant KSHV (rKSHV.219) was produced in Vero cells as previously described (Vieira and O'Hearn, 2004), or in latently-infected BJAB cells (BrK.219) (Kati et al., 2013) by inducing the lytic cycle using a combination of anti-IgM antibody (0.625 μg/ml, Southern Biotech) and TPA (12-O-Tetradecanoylphorbol 13-acetate, 0.05 μg/ml, Sigma-Aldrich) adapted from the protocol of Kati et al. (2015). KSHV produced in Vero cells was kindly provided by Prof D. J. Blackbourn (Guildford, UK) and BrK.219 cells were kindly gifted by Prof T. F. Schulz (Hannover, Germany). Titers of virus concentrates were determined by flow cytometric analysis of GFP-positive cells 48 hours after *in vitro* infection of Raji cells by EBV or HEK293T cells by KSHV on a FACSCanto II (BD Biosciences), as previously described (Antsiferova et al., 2014).

### Quantification of EBV and KSHV DNA

For humanized mouse samples, total DNA from whole blood or serum was extracted using the NucliSENS EasyMag System (bioMérieux) according to the manufacturer's protocol. DNA from spleen tissue was isolated using the DNeasy Blood & Tissue Kit (QIAGEN). Quantification of EBV BamHI W DNA was performed by TaqMan (Applied Biosystems) real-time PCR on an ABI Prism 7700 Sequence detector (Applied Biosystems) with the following primer and FAM/TAMRA-labeled probe sequence (modified from Berger et al., 2001): 5′-CTTCTCAGTCCAGCGCGTTT-3′, 5′-CAGTGGTCCCCCTCCCTAGA-3′, 5′-(FAM)-CGTAAGCCAGA CAGCAGCCAATTGTCAG-(TAMRA)-3′. KSHV ORF26 DNA was measured by TaqMan (Applied Biosystems) quantitative PCR on a C1000 Touch CFX384 Real-Time platform (Bio-Rad, Hercules, CA, USA) as previously described (McHugh et al., 2017) with the following primer and probe sequence (modified from Tedeschi et al., 2001): 5′-GCTCGAATCCAACGGATTTG-3′, 5′-AATA GCGTGCCCCAGTTGC-3, 5′-(FAM)-TTCCCCATGGTCGTGCCTC-(BHQ-1)-3′. Samples were analyzed in duplicates or triplicates.

For human samples, peripheral blood DNA was extracted using the DNeasy Blood & Tissue Kit (QIAGEN) according to the manufacturer's protocol and frozen at −20°C until use. EBV DNA was quantified by TaqMan (Applied Biosystems) real-time PCR targeting the BALF5 gene and normalized to β-actin, as described by Forconi et al. (2018) and Moormann et al. (2005). The previously determined threshold of 3 log EBV copies / μg DNA was used to group samples into the 2 groups: no / low EBV and high EBV.

### KSHV serology by multiplex beads assay

We used 7 KSHV recombinant open reading frames (ORFs): ORF59, ORF73/ latency-associated nuclear antigen (LANA), ORF65, ORF61, ORF38, K8.1, and K5. Bio-plex COOH carboxylated nonmagnetic beads ($1.25 \times 10^7$ microspheres/mL) were coupled to corresponding antigens at 100 μg/500 μL based on manufacturer's protocol, and antibody levels for KSHV, EBV, and malaria measured by BioPlex 200 Multianalyte Analyzer (Bio-Rad Laboratories) as previously described in Oluoch et al. (2020). In order to determine inter/intraassay variability, negative and positive control samples were included on each plate in duplicates. A comparison of the mean and standard deviation of duplicates within and between/across plates was used to determine the percent relative standard deviation (%RSD), which showed a range of 2%–15% for KSHV antigens. To determine individual seropositivity cutoffs, we used the receiver operating characteristic (ROC) curve analysis (Greiner et al., 2000) of the 7 KSHV antigens based on median fluorescence intensities (MFI) of 11 Africans and 15 North Americans adults with high and low risks of KSHV infection, respectively.

### Cell isolation

Spleen tissue was manually dissociated, filtered through 70-μm cell strainer, and subjected to Ficoll gradient centrifugation (Ficoll Paque Premiem, GE Healthcare). Liver tissue was digested for 30min at 37°C in buffer containing DNase (0.4mg/ml) and Collagenase D (20μg/ml) (Roche), followed by addition of 0.5M EDTA, filtering and separation of mononuclear cells on Percoll gradients. Whole blood was collected by tail-vein and terminal cardiac puncture in tubes containing heparin or EDTA. Prior to erythrocyte lysis by ACK lysis buffer, the white blood cell count in whole blood was determined with a hematology analyzer (Beckman Coulter AcT Diff Analyzer). Human PBMCs were isolated from Lithium-Heparin vacutainers by Ficoll gradient centrifugation within 2 hours of the blood draw and cryopreserved until use, as described by Forconi et al. (2018).

### Flow cytometric analysis

All antibodies are listed in the Key resource table. Dead cells were excluded using Fixable Viability dyes (Near-IR and Aqua, Biolegend). For surface stainings, single cell suspensions were incubated with fluorophore-conjugated antibodies for 30min at 4°C, washed and fixed with 1% PFA. For intracellular stainings, cells were fixed and permeabilized with the Cytofix/Cytoperm Kit (BD Bioscience) after surface antigen staining had been performed. Intranuclear stainings were performed after fixation and permeabilization with the Foxp3 staining kit (eBioscience) according to the manufacturer's instructions. Acquisition and compensation was performed on BD FACS Canto II, BD LSR II Fortessa and BD FACSymphony A5 flow cytometers. Data were exported and analyzed using FlowJo software (version 10, TreeStar Inc). For UMAP visualizations, FCS files of compensated, quality-controlled, single, live, human $CD45^+CD7^+Lin^-$ (CD3, CD4, CD19, CD14) cells were exported from FlowJo into the R environment (R Core Team, 2020) where data were arcsine-transformed using transformation cofactors determined in Cytobank (https://www.cytobank.org), followed by percentile normalization based on the workflow from Hartmann et al. (2016) and UMAP dimensionality reduction (McInnes et al., 2018; https://github.com/lmcinnes/umap) with the following parameters: n_neighbors = 20, n_components = 2, metric = ''euclidean,'', n_epochs = 250 and min_dist = 0.3. Heatmaps, graphs and pie charts were generated in R, using Prism (GraphPad Software) or SPICE software (Roederer et al., 2011).

### Functional assays

Single cell suspensions of liver and spleen tissue were cocultured with K562 or Raji cells at a ratio of 10:1 in RPMI 1640 (GIBCO, Thermo Fisher Scientific) with 10% FCS in a humidified incubator at 37°C and 5% $CO_2$. Culture medium contained FITC-labeled mouse anti-human CD107a (clone H4A3, BD Bioscience) antibody and monensin was added after 1 hour of coculture. For the ADCC assay, Raji cells were incubated with Rituximab (MabThera, Roche) at a concentration of 1μg/ml for 10min at 37°C prior to the addition of effector cells. For the stimulation with IL-12 (20ng/ml, Biolegend) and IL-18 (10ng/ml, Biolegend), the culture medium was supplemented with metalloproteinase inhibitor TAPI-1 (5 μg/ml, Tocris), and monensin and Brefeldin A was added after 1 hour of stimulation. After a total of 5 hours, cells were washed, stained, and analyzed on a BD LSR II Fortessa or BD FACSymphony A5 flow cytometers as described above.

### Histological staining

Spleen and liver sections were fixed in 4% formalin and paraffin-embedded (FFPE). Immunohistochemical single staining of EBNA2 (clone PE2, Abcam) and LANA (clone LN53, Clinisciences) was carried out on a Leica BOND-III automated immunohistochemistry system using diaminobenzidin (DAB) as chromogen (Zytomed Systems, Berlin, Germany). *In situ*-hybridization for the detection of EBER was performed as described previously (Meyer et al., 2011) with DAP as substrate. Multiplex immunofluorescence (IF) staining was performed on FFPE tissue using Opal dyes and Spectral DAPI (FP1490) from PerkinElmer. Opal dyes 520, 540, 620 and 690 were used to detect EBNA2 (clone PE2, Abcam), CD20 (clone SP32, Cell Marque), LANA (clone LN53, CliniSciences) and IRF4/Mum1 (clone: MUM1p, CliniSciences), respectively. Single stains were used to compensate overlapping spectras. Staining was quantified on a Vectra3 automated quantitative pathology imaging system using Vectra, Phenochart (v1.0) and InForm (v2.4.8) software (all from PerkinElmer), as previously described (Murer et al., 2018).

### Serum cytokine quantification

Serum of huNSG mice was collected upon terminal cardiac puncture using BD Mictrotainer tubes and frozen at −20°C until use. Samples were assayed for cytokines using the Meso Scale Discovery (Meso Scale Diagnostics, Rockville, MD) U-PLEX (Biomarker Group 1 Human, K15067L) and V-PLEX (Proinflammatory Panel 1 Human Kit, K15049D) platform following the manufacturer's recommendations. Plates were read on a Meso QuickPlex SQ120 and analyzed with Discovery Workbench 4.0.12, both from Meso Scale Discovery. Samples and calibrator dilutions for the standard curves were run in duplicates. Heatmaps were generated in R using the *superheat* package (Barter and Yu, 2018) after empirical percentile transformation of cytokine levels (*heatmaply* package; Galili et al., 2018).

Plasma from Kenyan children samples was isolated from whole blood and kept frozen until use. IL-18 concentration in plasma of Kenyan children was measured using Human IL-18 Simplex ProcartaPlex from eBiosciences (cat#EPX01A-10267-901, lot#144494103, ULOQ/LLOQ of 49500/12 pg/ml). The assay was performed following the manufacturer's protocol and run on a Bio-Plex 200 (Biorad) platform using the Bioplex Manager Software (Biorad, version 6.1). The concentration of the samples was calculated by plotting the expected concentration of the standards against the MFI generated by each standard using a5PL algorithm.

## QUANTIFICATION AND STATISTICAL ANALYSIS

Survival curves were analyzed by log-rank test. Contingency tables of categorical data were examined by two-tailed Fisher's exact test. Correlation was assessed by Spearman's rank test. The D'Agostino & Pearson omnibus test was used to test the normal distribution of data. Unpaired non-parametric data were analyzed by Mann-Whitney U test or by Dunn's multiple comparison test following Kruskall Wallis test when comparing more than two groups. Paired non-parametric data were analyzed by Wilcoxon signed-rank test or by multiple comparison tests following Friedmann's test when comparing more than two groups. Paired parametric data were analyzed by repeated-measures ANOVA or by fitting a mixed model (REML) in case of missing values, followed by Fisher's LSD post hoc test. P values from follow-up multiple comparison tests are FDR-adjusted. A p or FDR-adjusted q value of $< 0.05$ was considered statistically significant. All statistics were computed with GraphPad Prism 8 (GraphPad Software, San Diego, CA) and details can be found in figures or in corresponding legends.